

การพัฒนารอยแตกในการทดลองความดันสูงของหินดินดานบริเวณรัฐเท็กซัส
ประเทศสหรัฐอเมริกา

นายธนพงศ์ วาณิชยน์ทิ

โครงการนี้เป็นส่วนหนึ่งของการศึกษาตามหลักสูตรวิทยาศาสตรบัณฑิต
ภาควิชาธรณีวิทยา คณะวิทยาศาสตร์ จุฬาลงกรณ์มหาวิทยาลัย
ปีการศึกษา 2559

FRACTURE DEVELOPMENT IN HIGH PRESSURE EXPERIMENT OF SHALE
IN TEXAS, USA

Mr. Thanapong Vanichnatee

A Project Submitted in Partial Fulfillment of the Requirements
for the Degree of Bachelor of Science Program in Geology
Department of Geology, Faculty of Science, Chulalongkorn University
Academic Year 2016

Project Title	FRACTURE DEVELOPMENT IN HIGH PRESSURE EXPERIEMNT OF SHALE IN TEXAS, USA
By	Mr. Thanapong Vanichnatee
Field of Study	Geology
Project Advisor	Dr. Waruntorn Kanitpanyacharoen

Submitted date

____/____/____

Approval date

____/____/____

(Dr. Waruntorn Kanitpanyacharoen)

Project Advisor

ธนพงศ์ วาณิชยน์ที่ : การพัฒนารอยแตกในการทดลองความดันสูงของหินดินดานบริเวณรัฐเท็กซัส ประเทศสหรัฐอเมริกา. (FRACTURE DEVELOPMENT IN HIGH PRESSURE EXPERIMENT OF SHALE IN TEXAS, USA) อ.ที่ปรึกษาโครงการงาน : ดร.วรัญทร คณิตปัญญาเจริญ, 62 หน้า.

หินดินดานที่มีสารอินทรีย์เป็นองค์ประกอบในปริมาณมาก มักจะเป็นหินต้นกำเนิดในแหล่งกักเก็บปิโตรเลียม ซึ่งในปัจจุบัน หินดินดานประเภทนี้ถูกขุดเจาะเพื่อนำก๊าซธรรมชาติขึ้นมาใช้ได้โดยตรงด้วยการใช้เทคโนโลยีการขุดเจาะในแนวระนาบ ผสมผสานกับการอัดของไหลด้วยแรงดันสูงเพื่อสร้างรอยแตกในหินดินดาน แม้ว่าเทคโนโลยีนี้จะช่วยผลิตก๊าซธรรมชาติจากหินดินดานได้มาก แต่การประเมินศักยภาพของหินดินดานเป็นเรื่องที่ยาก เนื่องจากโครงสร้างหินดินดานมีความซับซ้อนโดยเฉพาะในเรื่องคุณสมบัติของรูพรุนและรอยแตก ซึ่งเป็นหนึ่งในปัจจัยสำคัญที่ส่งผลต่อการไหลของปิโตรเลียม การศึกษานี้จึงมีจุดมุ่งหมายเพื่อจำลองสภาวะความร้อนและความดันสูงของการอัดแรงดันในชั้นหินดินดานใต้ผิวโลก และศึกษาลักษณะโครงสร้างจุลภาคโดยเฉพาะลักษณะของรูพรุนและรอยแตกรวมทั้งปริมาณความเค้นและความเครียดของแร่จากชั้นหินดินดานบาร์เน็ตต์ รัฐเท็กซัส ประเทศสหรัฐอเมริกา เครื่องอัดแรงดันสูงจะถูกใช้เพิ่มความดันและความร้อนให้กับตัวอย่างหินดินดานสูงถึง 240 เมกะพาสคาล และ 100 องศาเซลเซียส ร่วมกับการใช้วิธีเลี้ยวเบนของรังสีเอ็กซ์ซินโครตรอน เพื่อศึกษาการเปลี่ยนแปลงขององค์ประกอบภายในหินดินดาน นอกจากนี้ยังใช้วิธีถ่ายภาพตัดขวางด้วยรังสีเอ็กซ์ซินโครตรอน เพื่อศึกษาโครงสร้างสามมิติของรูพรุนขนาดเล็ก รอยแตก และสารอินทรีย์ของหินดินดาน จากการศึกษาพบว่าตัวอย่างหินดินดานประกอบด้วยแร่ควอตซ์ประมาณร้อยละ 35 และแร่ดินประมาณร้อยละ 56 โดยเฉพาะแร่โอลิโอสไมท์และแร่โอลิโอสเมกไทต์ เมื่อแร่แต่ละชนิดถูกอัดด้วยแรงดันสูงก็จะได้รับความเค้นที่ไม่เท่ากันในแต่ละทิศทาง แร่โอลิโอสเมกไทต์มีค่าความแตกต่างของความเค้นระหว่างแนวที่สูงสุดและต่ำสุดอยู่ในปริมาณสูงสุดซึ่งหมายความว่า แร่ชนิดนี้มีความต้านทานต่อแรงที่ได้น้อยที่สุด ในขณะที่แร่ควอตซ์เป็นแร่ที่มีความต้านทานต่อแรงที่ได้น้อยที่สุด นอกจากนี้ผลการศึกษายังแสดงให้เห็นว่าลักษณะและการกระจายตัวของรูพรุน รอยแตกและสารอินทรีย์มีการเปลี่ยนแปลงไปอย่างมากหลังจากทำการทดลองอัดด้วยแรงดันสูง ปริมาณรูพรุนก่อนทำการอัดมีอยู่ประมาณร้อยละ 3 ซึ่งรูพรุนมักจะมีขนาดเล็กและรูปร่างเป็นทรงกลม แต่หลังจากทำการอัดรูพรุนส่วนใหญ่ถูกเชื่อมต่อกันเป็นแนวรอยแตกหลายแนว ซึ่งแนวรอยแตกหลักประกอบด้วย 2 แนวและทำมุมกับระนาบการเรียงตัวของหินดินดาน ที่วางตัวในแนวเดียวกับทิศทางของความเค้นหลัก พบว่าค่าเฉลี่ยของมุมระหว่างรอยแตกและระนาบการเรียงตัวของหินมีค่าประมาณ 26 องศา ซึ่งการเกิดรอยแตกเหล่านี้ส่งผลทำให้ค่าความซึมผ่านของหินดินดาน เพิ่มขึ้นเป็น 6.4 ถึง 9.3 มิลลิเดาร์ซี ผลลัพธ์ที่ได้จากการศึกษานี้ช่วยเพิ่มความรู้ความเข้าใจให้กับลักษณะรอยแตกที่เกิดในสภาวะที่มีความดันและความร้อนสูง และสามารถนำไปเป็นต้นแบบในการศึกษาลักษณะการแตกของหินดินดานจากแอ่งอื่นๆ ในอนาคตได้

ภาควิชา _____ ธรณีวิทยา _____ ลายมือชื่อนิสิต _____
 สาขาวิชา _____ ธรณีวิทยา _____ ลายมือชื่ออาจารย์ที่ปรึกษา _____
 ปีการศึกษา _____ 2559 _____

5632712423 : MAJOR GEOLOGY

KEYWORDS : HYDRAULIC FRACTURING / FRACTURE / STRESS / STRAIN / STIFFNESS / ELASTIC PROPERTIES / SYNCHROTRON X-RAY DIFFRACTION / SYNCHROTRON X-RAY MICRO TOMOGRAPHY / PERMEABILITY / D-DIA

THANAPONG VANICHNATEE : FRACTURE DEVELOPMENT IN HIGH PRESSURE EXPERIMENT OF SHALE IN TEXAS, USA. ADVISOR : DR. WARUNTORN KANITPANYACHAROEN, 62 pp.

Organic-rich shale has been generally considered as a source rock in hydrocarbon reservoir. With the advancement of horizontal drilling and hydraulic fracturing techniques, recently shale formation can be directly extracted for hydrocarbon. Despite the extensive studies of shale characteristics, there is little information about mechanical behavior and fracture system of shale during hydraulic fracturing process. This study thus aims to simulate the high pressure and high temperature conditions of hydraulic fracturing process and investigate microstructural and mechanical changes of the Barnett Shale from Texas, USA. The multi-anvil press D-DIA apparatus equipped with synchrotron X-ray diffraction (SYN-XRD) technique is used to compress shale to 240 MPa while simultaneously heated to 100 °C, and monitor compositional various. Moreover, synchrotron X-ray tomographic microscopy (SYN-MCT) is further used to investigate three-dimensional (3D) fractures, pores, and organic material (kerogen) of compressed shale. SYN-XRD results show that the sample is mainly composed of quartz (~35%), illite-mica (~28%), and illite-smectite (~25%). Minor minerals include kaolinite (~3%) and pyrite (~9%). Upon compressing sample, the volumes of illite-smectite decrease due to dehydration. Differential stresses of clay minerals and quartz are determined from diffraction patterns, suggesting illite-smectite is the least stiff mineral due to the highest differential stress (~2-3 GPa) whereas quartz is the most stiff one. In addition, SYN-MCT results provide the 3D morphology and distribution of pore, fracture, and kerogen. Pores (~3 vol.%) are mostly rounded and scattered in the sample while kerogen is (~15 vol.%) mostly elongated and aligned parallel with pores. Upon compression, fractures start to develop and become prominent (1.27 vol.%) while unloading, propagating intersect the principal stress direction at the average angle of 26°. Permeability is calculated from these fractures, ranging from 6.4 to 9.3 mD.

Department : Geology Student's Signature _____
 Field of Study : Geology Advisor's Signature _____
 Academic Year : 2016

ACKNOWLEDGEMENTS

First of all, I would like to appreciate wholeheartedly to my advisor, Dr. Waruntorn Kanitpanyacharoen, who is always teaching me with her sedateness, encouraging me when I faced up with the tensing problem and supporting me in very decision that I made. I would like to thank her for every advice and encouragement throughout the research. Furthermore, I would also like to thank to the Mineral and Rock Physics team for teaching all processes and useful functions in MAUD software and Segmentation program, for the great discussions, and the cheering up throughout research.

Moreover, I would like to give thanks for all teachers in Department of Geology, Chulalongkorn University, who had been teaching me since when I was a freshman not only the geological lessons but also the life-lessons.

And I take this opportunity to gratefully thank Chevron Thailand, the AAPG Foundation, and the SPE Thailand section who had been giving the scholarship and grant for me over 4 years.

In addition, thank you to my lovely Geo'57 friends for the support and encouragement in the past few years.

And last but not least, I appreciate my heartwarming family especially my mother and father who are my role model since I was young. Thank you to your understanding, supporting and taking care of me. Very achievements in my life are because of your raising. Thank you for everything !

CONTENTS

	Page
ABSTRACT (THAI)	iv
ABSTRACT (ENGLISH)	v
ACKNOWLEDGEMENTS	vi
CONTENTS	vii
LIST OF FIGURES	ix
LIST OF TABLES	xiv
CHAPTER I INTRODUCTION	1
1.1 Background	1
1.2 Literature Review	1
1.3 Objective	6
CHAPTER II GEOLOGY OF STUDY AREA	7
2.1 Structural evolution and general stratigraphy of the Fort Worth Basin	7
2.2 Barnett Shale deposition	11
2.3 Petroleum geochemistry and Thermal history of Barnett Shale	20
CHAPTER III METHODOLOGY	24
3.1 Laboratory phase	24
3.1.1. Sample preparation	24
3.1.2. Before compression	25
3.1.3. During compression	25
3.1.4. After compression	26
3.2 Data analysis phase	26
3.2.1. Material Analysis Using Diffraction (MAUD)	26
3.2.2. Segmentation program	36
CHAPTER IV RESULTS	38
4.1 Radiograph images	38
4.2 Plot and Plot 2D	43
4.3 Mineralogy	44

	Page
4.4 Cell parameters	45
4.5 Preferred orientation	46
4.6 Macrostress and differential stress	46
4.7 Elastic property	48
4.8 Three-dimensional microstructure	49
4.9 Permeability from 3D mathematic simulation microstructure model	51
CHEPTER V DISCUSSION AND CONCLUSIONS	52
5.1 Discussion	52
5.1.1. Proportion of illite-mica and illite-smectite	52
5.1.2. Stiffness of minerals	53
5.1.3. Fracture development	53
5.1.4. Fracture angle	56
5.2 Conclusions	57
REFERENCES	59

LIST OF FIGURES

	Page
<p>Figure 1.1 the left side illustrates the apparatus (Wang <i>et al.</i>, 2003) and the right side shows the real D-DIA, pressure transmitting media, and sample.</p>	2
<p>Figure 1.2 illustrates the procedure of synchrotron x-ray diffraction technique. The source of incident beam is from synchrotron and each lattice plane of each mineral diffracts a Debye-Scherrer rings (http://pd.chem.ucl.ac.uk).</p>	3
<p>Figure 1.3 shows diffraction image composing of Debye-Scherrer rings (Wenk <i>et al.</i>, 2003).</p>	3
<p>Figure 1.4 3D representation of an unrolled image from diffraction image in Figure 1.3 (Wenk <i>et al.</i>, 2003).</p>	4
<p>Figure 1.5 shows schematic diagram of the synchrotron x-ray micro tomography (Kanitpanyachoen <i>et al.</i>, 2012).</p>	5
<p>Figure 1.6. shows a workflow of data reconstruction (Kanitpanyachoen <i>et al.</i>, 2012).</p>	5
<p>Figure 1.7 (a) shows 2D reconstructed image and (b) shows grayscale values of Figure 1.7a which is selected threshold of each material based on its absorption value (Kanitpanyachoen <i>et al.</i>, 2012).</p>	5
<p>Figure 2.1 Generalized structure contour map, top of Ellenburger Group, Bend arch - Fort Worth Basin area of north-central Texas. Data interpreting from subsurface log and IHS well-history database (IHS Energy, 2003)</p>	8

	Page
<p>Figure 2.2 (A) Maps shows area of U.S. Geological Survey (USGS) province 45 (termed the “Bend arch – Fort Worth Basin province”), geographic extent of the Mississippian Barnett Shale, major structural features, and Newark East and Boonsville fields. (B) Map shows boundary of Barnett-Paleozoic total petroleum system and major structure elements in the Bend arch – Fort Worth Basin province (Pollastro <i>et al.</i>, 2007).</p>	9
<p>Figure 2.3 Generalized subsurface stratigraphic section of the Bend arch – Fort Worth Basin province showing distribution of source rocks, reservoir rocks, and seal rocks of the Barnett-Paleozoic total petroleum system (Pollastro <i>et al.</i>, 2007).</p>	12
<p>Figure 2.4 Map showing regional extent of Barnett Shale, thickness of Barnett Shale, isopachs of Barnett Shale, and lines of well-log cross sections AA’ of Figure 2.7 and BB’ of Figure 2.8. Contour intervals are 50 ft (15 m) for thicknesses from 0 to 300 ft (0 to 91 m) and 100 ft (30 m) for thicknesses from 300 to 1000 ft (91 to 305 m) (Pollastro <i>et al.</i>, 2007).</p>	13
<p>Figure 2.5 Paleogeographic maps of north Texas and southwestern Oklahoma during the Mississippian. (A) The Osagean showing incipient subduction zone and consequent uplift adjacent to present-day Fort Worth Basin and areas of deposition of the lower part of the Barnett Shale (dark shading), position of the Chappel shelf and bioherm deposition. Emergent areas are lightly shaded. (B) The Chesterian showing major structural features and area of upper Barnett Shale, or equivalent, deposition (dark shading). Emergent areas are light shaded (Pollastro <i>et al.</i>, 2007).</p>	14
<p>Figure 2.6 Typical well-log stratigraphic section showing gamma-ray and resistivity logs through the Barnett Shale and overlying and underlying units. Depth in feet (Pollastro <i>et al.</i>, 2007).</p>	15

	Page
Figure 2.7 Generalized southwest-northeast stratigraphic cross section AA' based on well-log correlations; line of section is from Figure 2.4. Gamma-log profile (red) and resistivity-log profile (yellow) are shown for reference on selected wells (Pollastro <i>et al.</i> , 2007). Not to scale horizontally.	16
Figure 2.8 Generalized northeast-southwest stratigraphic cross section BB' based on well-log correlations; line of section is from Figure 2.4. Gamma-log profile (red) and resistivity-log profile (yellow) are shown for reference on selected wells (Pollastro <i>et al.</i> , 2007). Not to scale horizontally.	17
Figure 2.9 Isopach maps of limestone units in Barnett Shale. (A) Lime wash units within the Barnett Shale, Fort Worth Basin, Texas. Contour interval equals 25 ft (8 m). (B) Forestburg limestone within the Barnett Shale, Fort Worth Basin, Texas. Contour interval equals 25 ft (8 m) (Pollastro <i>et al.</i> , 2007).	18
Figure 2.10 Isopach map of the upper Barnett Shale unit, Fort Worth Basin, Texas (Pollastro <i>et al.</i> , 2007).	19
Figure 2.11 shows lines of equal thermal maturity map as determined from mean vitrinite reflectance (R_o) of Barnett Shale. Areas of probable high hydrothermal heating and anomalously high R_o are also indicated (arrows) (Pollastro <i>et al.</i> , 2007).	21
Figure 2.12 shows relation between oil and gas production from Barnett Shale in Fort Worth Basin versus oil- and gas-generation windows as determined from mean vitrinite reflectance (R_o) (See Figure 2.11) (Pollastro <i>et al.</i> , 2007).	22
Figure 2.13 Petroleum system events chart for Barnett-Paleozoic total petroleum system of the Fort Worth Basin. Abbreviations: E = early; M = middle; L = late; Cam = Cambrian; Ord = Ordovician; Sil = Silurian; Dev = Devonian; Mis = Mississippian; Pen = Pennsylvanian; Per = Permian; Tr = Triassic; Jur = Jurassic; Cret = Cretaceous; Ter = Tertiary; Cen = Cenozoic; O = Oligocene; Mi = Miocene (Pollastro <i>et al.</i> , 2007).	23
Figure 3.1 shows values of parameters in image properties.	26

	Page
Figure 3.2 shows values of parameters in Centralize and Intergrate Debye-Scherrer Rings.	27
Figure 3.3 shows plot 2D of time period 001 lacking data in 18 intergrated angle.	28
Figure 3.4 shows Computation range.	28
Figure 3.5 shows parameters in Diffraction Instrument.	29
Figure 3.6 shows parameters in Flat Image in transmission/reflection angular calibration.	30
Figure 3.7 shows parameters in Source from Synchrotron.	30
Figure 3.8 shows parameters in Background peaks at position 0 eta.	31
Figure 3.9 shows parameters in Background peaks at position 170 eta.	31
Figure 3.10 shows parameters in Background peaks at position 340 eta.	32
Figure 3.11 shows mineral and Pressure Transmitting Medium CIF files used in these study.	33
Figure 3.12 shows changed space group of illite-mica.	33
Figure 3.13 shows parameters in E-WIMV method for illite-mica, illite-smectite, and kaolinite.	35
Figure 4.1 shows parameters used for calculating %Strain.	41
Figure 4.2 shows graph of compressional strate and %Strain versus time periods.	42
Figure 4.3 shows 1D X-ray diffraction pattern (A) and 2D Plot (B) of time period 001.	43
Figure 4.4 shows graph plotting values between differential stress (GPa) and %Strain.	48
Figure 4.5 shows microstructures and textures before compression composing of pores, kerogen, and pyrite.	49
Figure 4.6 shows microstructures and textures after compression composing of fractures and pyrite.	49
Figure 4.7 shows 3D microstructure model before compression which composes of scattered pores.	50

	Page
Figure 4.8 shows 3D microstructure model after compression which composes of huge fractures (Pores are not shown in this picture).	50
Figure 4.9 shows composition variation before and after compression.	51
Figure 5.1 shows graph of vol.% of illite-mica and illite-smectite.	52
Figure 5.2 shows the first state of fracture development: Closure of existing cracks (dark blue).	54
Figure 5.3 shows the second state of fracture development: growth of cracks (red).	54
Figure 5.4 shows the third state of fracture development: cracks connection (red).	55
Figure 5.5 shows the third state of fracture development: fractures observed (red), permeability increases.	55
Figure 5.6 shows angle between fractures and major principle stress (Zhang, 2015).	56
Figure 5.7 shows angle between fractures and major principle stress of this study.	57

LIST OF TABLES

	Page
Table 3.1 shows state conditions and anvils status of the samples	25
Table 3.2 shows stiffness of illite-mica, illite-smectite, kaolinite, and quartz.	35
Table 4.1 shows radiographic images upon time periods.	38
Table 4.2 shows %Strain of each time period.	41
Table 4.3 The detail of phase volume and weight fraction of those samples.	44
Table 4.4 shows parameters of cell parameter.	45
Table 4.5 shows Pole densities for (100) pole figures of illite-mica and illite-smectite and (001) pole figure of kaolinite (m.r.d.)	46
Table 4.6 shows differential stress of minerals upon time periods.	47
Table 4.7 shows permeability of x and y axis	51

CHAPTER I

INTRODUCTION

1.1 Background

In the present, there is a development in population, technology, communication and logistics. Inescapably, for these factors make demand from using national resources increase dramatically, especially, restrictly national resources such as petroleum. Certainly, the more using this resource, the less having petroleum reserves in the reservoir.

For supporting the demand from increasingly using petroleum, nowadays, there is a high technology called “Hydraulic Fracturing” which is a new method for directly producing natural gas from source rock or generally known as shale. By injection high pressured fluid into the rock brings about the new fractures. The natural gas located along that fracture can lead out to the production well. On the contrary, using this technology makes the new fractures beneath the earth surface. Accordingly, we cannot see and estimate the characteristic and behavior of those fractures.

For better understanding and new knowledge about fractures development in high pressure under the earth surface of shale lead to this research in order to simulate the newly develop fracture occurring in the rock. Including, the quality, direction and distribution of the fractures are investigated in this research as well. Moreover, natural gas production by Hydraulic Fracturing is not widely studied in Thailand. So, this research can apply to produce petroleum in Thailand.

1.2 Literature Review

Wang *et al.*, 2003 had been developing a new apparatus which is called the deformation-DIA (D-DIA) (Figure 1.1) for high temperature condition and triaxial deformation to pressures up to 15 GPa, based on the widely used cubic-anvil apparatus, DIA.

This study used D-DIA apparatus which has 6 anvils made from Tungsten Carbide, this material is high resistant to deformation by an applied force and temperature, compressing the sample directly in 6 directions to pressures up to 240 MPa and heat sample up to 100 °C so as to simulate shale formation beneath surface. Between anvils and sample, we used pressure transmitting medium which can slowly transmit pressure from anvils to sample and protect crashing between those anvils. There is a tiny space between each anvil for passing of incoming x-ray and diffracted x-ray to investigate mineralogy during the compression. Moreover, we can measure strains by x-ray radiographic imaging of the sample from diffracted x-ray during the compression.

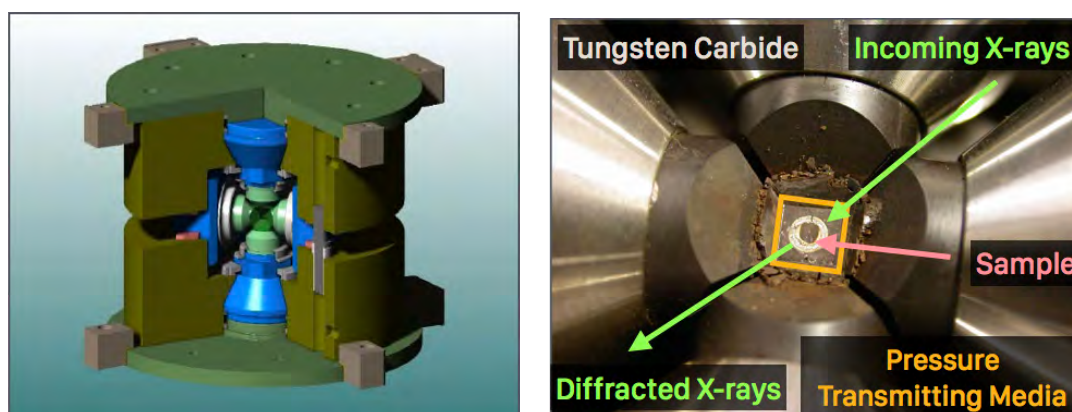


Figure 1.1 the left side illustrates the apparatus (Wang *et al.*, 2003) and the right side shows the real D-DIA, pressure transmitting media, and sample.

To investigate minerals composition, preferred orientation, and differential stress of each mineral during the compression, diffraction images from the synchrotron x-ray diffraction (SYN-XRD) technique were used in this study (Figure 1.2) and those images (Figure 1.3, 1.4) were analyzed by Material Analysis Using Diffraction (MAUD) based on the Rietveld refinement (Lutterotti *et al.*, 2013, Wenk *et al.*, 2014).

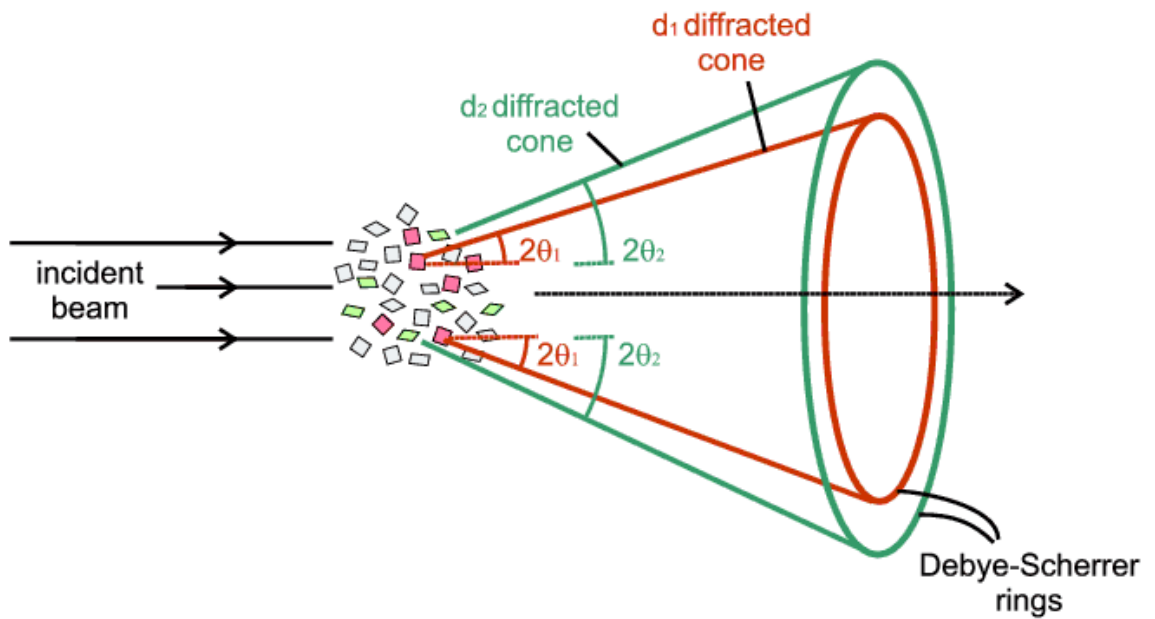


Figure 1.2 illustrates the procedure of synchrotron x-ray diffraction technique. The source of incident beam is from synchrotron and each lattice plane of each mineral diffracts a Debye-Scherrer rings (<http://pd.chem.ucl.ac.uk>).

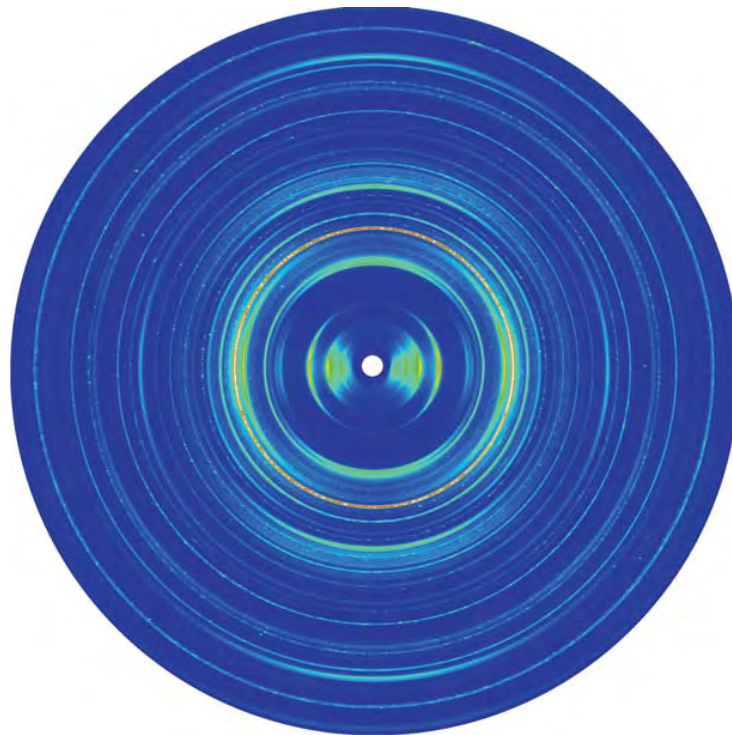


Figure 1.3 shows diffraction image composing of Debye-Scherrer rings (Wenk *et al.*, 2003).

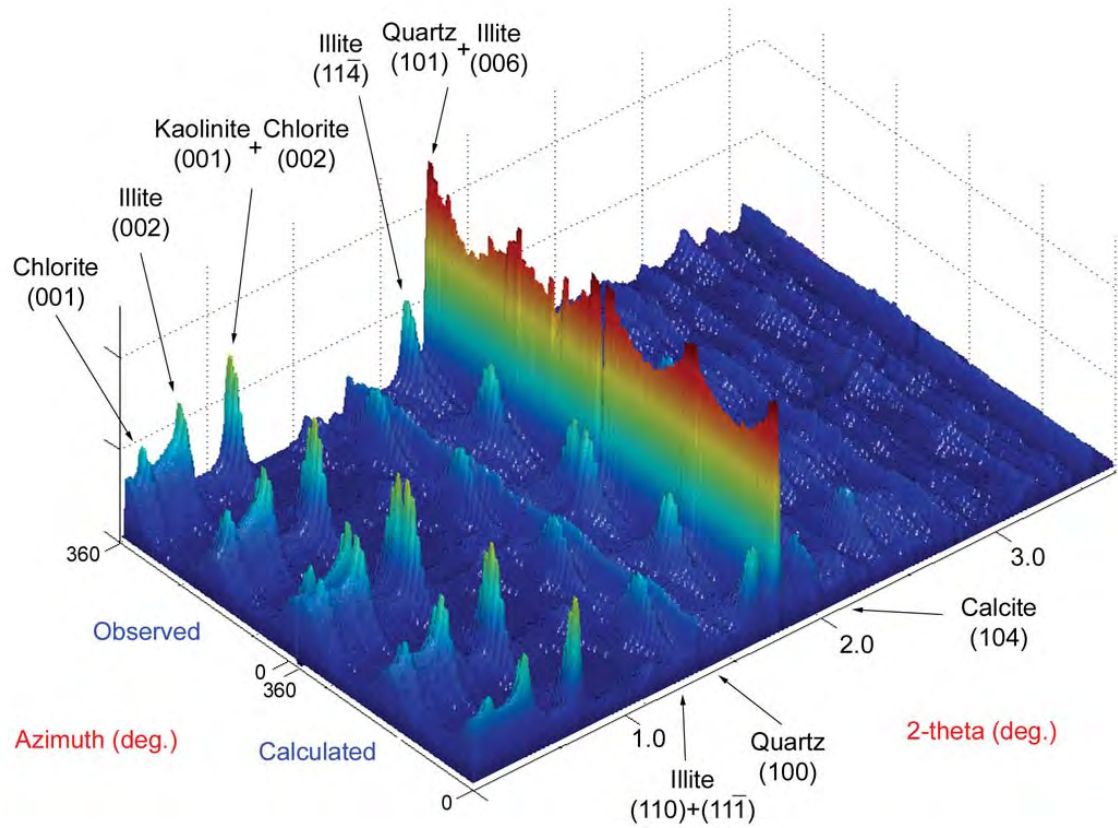


Figure 1.4 3D representation of an unrolled image from diffraction image in Figure 1.3 (Wenk *et al.*, 2003).

Moreover, to determine physical characteristics and to understand fracture development especially their distribution and volumes of pore, kerogen, and fracture, the Synchrotron X-ray Micro-tomography (SYN-MCT) technique (Figure 1.5, 1.6) was used to reconstruct three-dimensional data (Kanitpanyachoen *et al.*, 2013) before and after compression based on their x-ray absorption values (Figure 1.7).

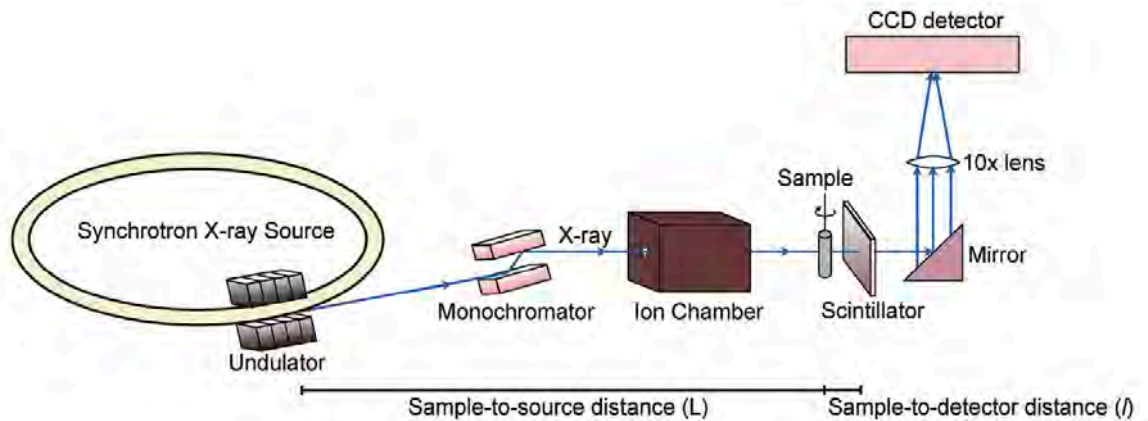


Figure 1.5 shows schematic diagram of the Synchrotron X-ray Micro-tomography (Kanitpanyachoen *et al.*, 2012).

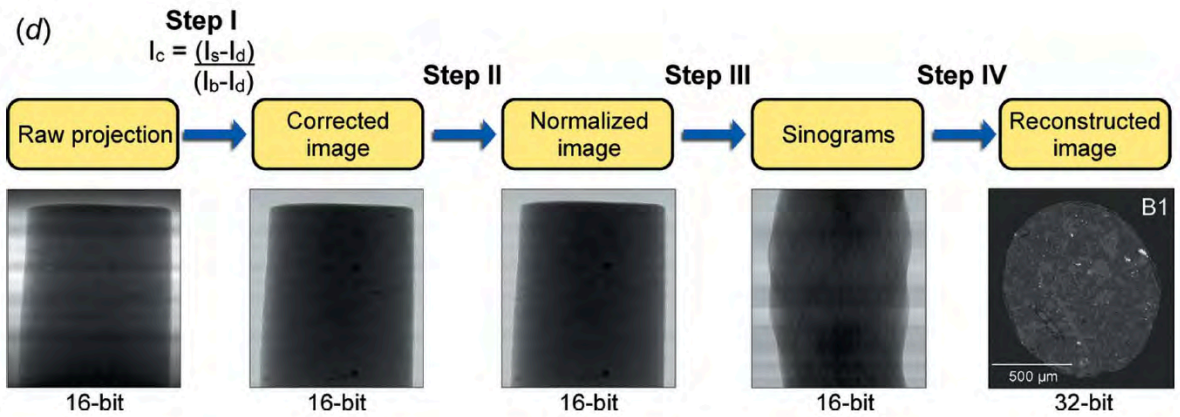


Figure 1.6. shows a workflow of data reconstruction (Kanitpanyachoen *et al.*, 2012).

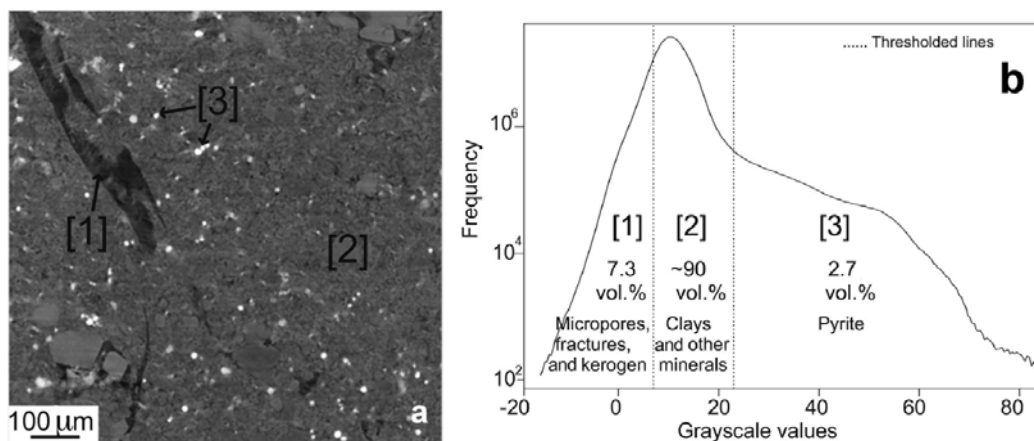


Figure 1.7 (a) shows 2D reconstructed image and (b) shows grayscale values of Figure 1.7a which is selected threshold of each material based on its absorption value (Kanitpanyachoen *et al.*, 2012).

1.3 Objective

To investigate compositional variation and fracture behavior of shale especially their morphology, distribution, and volumes under simulated high pressure and high temperature conditions.

CHAPTER II

GEOLOGY OF STUDY AREA

The corrected sample used in this study is from the Barnett Shale in Bend arch – Fort Worth Basin located in the north-central Texas, USA. This basin is the first place which has the achievement in unconventional petroleum producing in the world. And this basin is also the most significant oil and gas producing in this state.

The Barnett Shale is the primary source rock in the Mississippian age for oil and gas produced from Paleozoic reservoir rocks. Petroleum geochemistry and well logs data support that the Barnett Shale is organic-rich and thermally mature for hydrocarbon generation over most of this basin.

2.1 Structural evolution and general stratigraphy of the Fort Worth Basin

The Fort Worth Basin located in the north-central Texas which is estimated area about 38,000 km². The basin is a wedge-shaped, elongates in north-south trend and deeply depresses in northward (Figure 2.1). It is a foreland basins formed during the late Paleozoic Ouachita orogeny (Walper, 1982; Thompson, 1988).

The general structure in this basin is associated to the Ellenburger Group structure contour map (Figure 2.1). The northern and north-eastern most basin is bounded by the Red River and Muenster arches formed by reactivation of basement faults during Ouachita compression (Walper 1977, 1982) then southward to almost parallel the Ouachita thrust front which is the eastern boundary of the basin.

The Bend arch is a north-plunging positive subsurface structure located extended northward from the Llano uplift (Figure 2.2). The domal Llano uplift exposes Precambrian – Pennsylvanian rocks and bounds the basin in the south. Moreover, there is the Lampasas arch which is a secondary structural feature of the basin (Figure 2.2B).

An important structural feature, the Mineral Wells fault trending in northeast-southwest, cuts across the Newark East field which is a potential petroleum production area and locates in the north-eastern part of the basin (Figure 2.2). The fault system

may be called as the Mineral Wells – Newark East fault system. Its origin has been poorly understood because it is associated with neither the fault blocks of the Muenster and Red River arches nor the Ouachita thrusting.

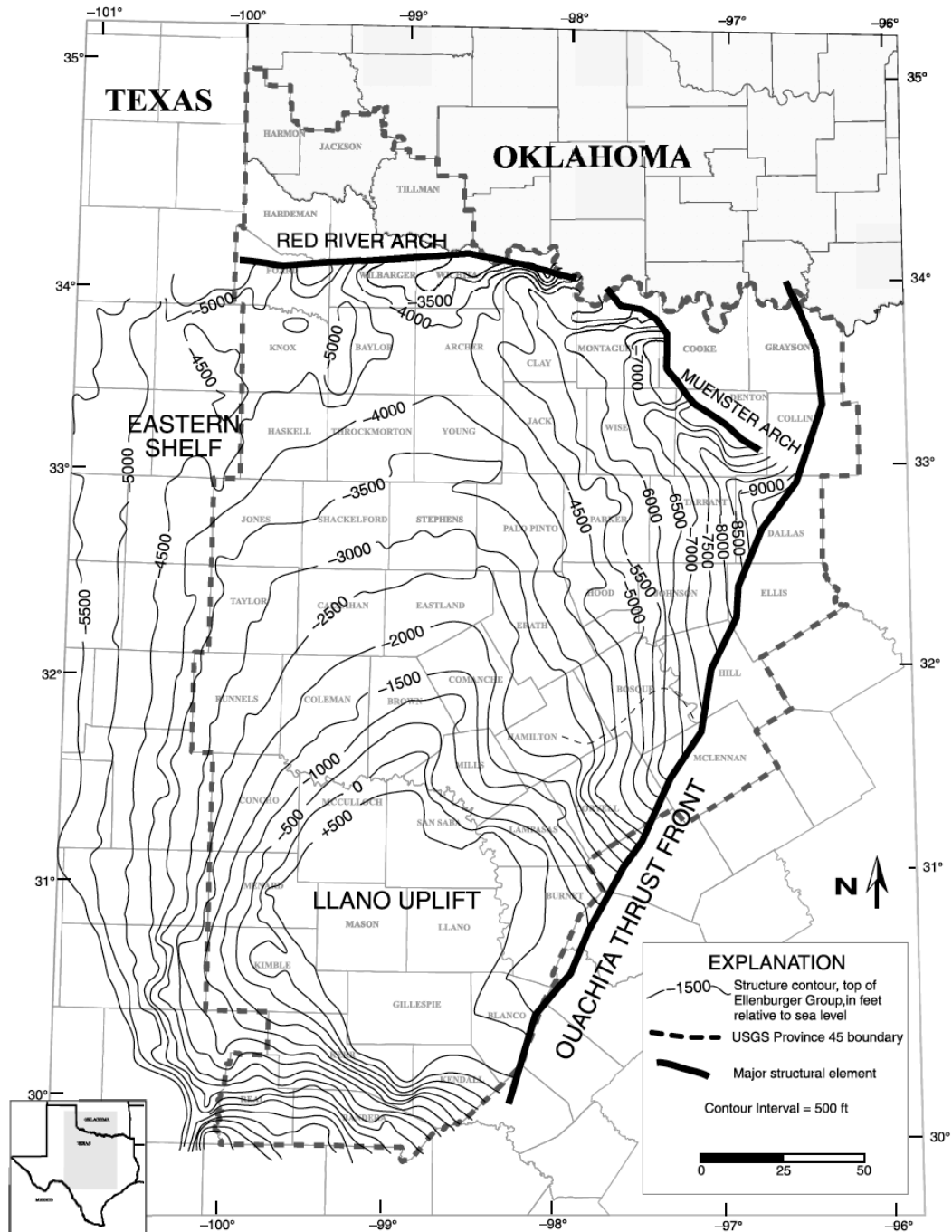


Figure 2.1 Generalized structure contour map, top of Ellenburger Group, Bend arch - Fort Worth Basin area of north-central Texas. Data interpreting from subsurface log and IHS well-history database (IHS Energy, 2003)

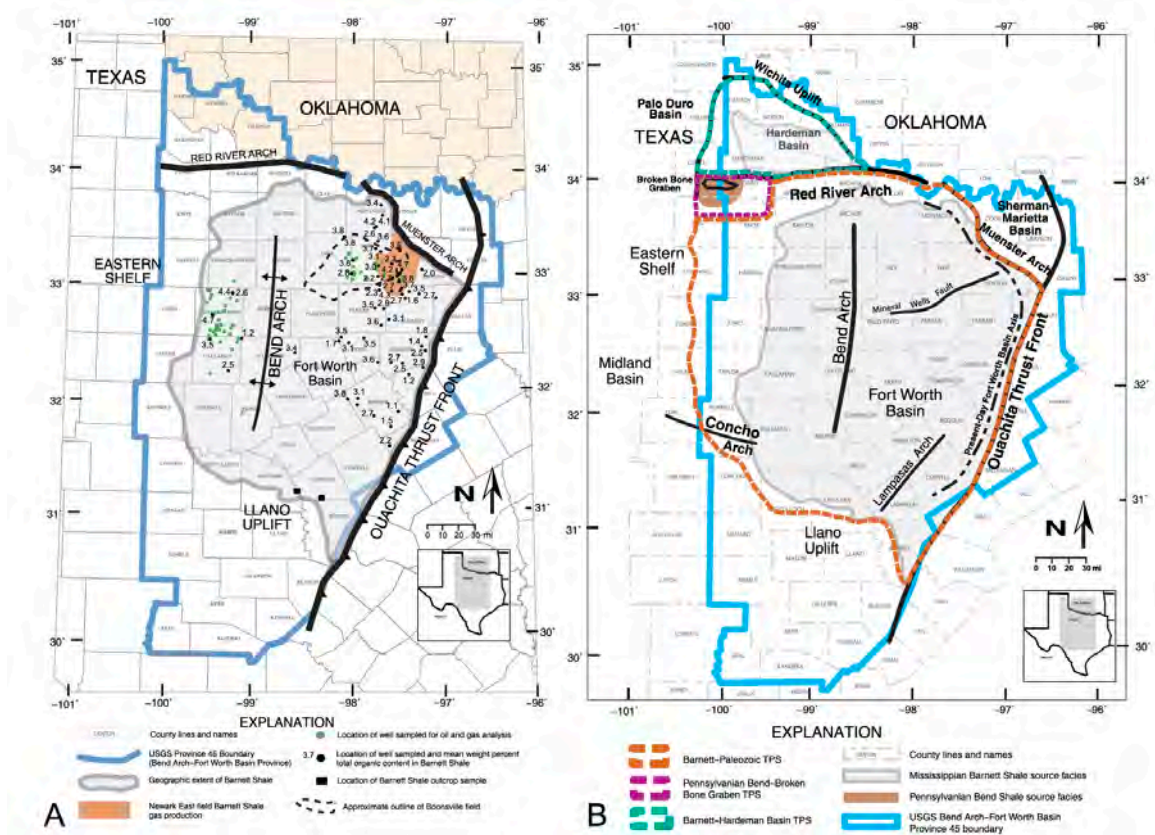


Figure 2.2 (A) Maps shows area of U.S. Geological Survey (USGS) province 45 (termed the “Bend arch – Fort Worth Basin province”), geographic extent of the Mississippian Barnett Shale, major structural features, and Newark East and Boonsville fields. (B) Map shows boundary of Barnett-Paleozoic total petroleum system and major structure elements in the Bend arch – Fort Worth Basin province (Pollastro *et al.*, 2007).

The previous studies suggested that the Mineral Wells - Newark East fault system has a significant factor in (1) the deposition of Bend Group conglomerates (Thompson, 1982); (2) effecting depositional patterns and thermal history of the Barnett Shale (Bowker, 2003; Pollastro *et al.*, 2004a; Montgomery *et al.*, 2006); (3) controlling migration and distribution of oil-associated gas at Boonville field in the northern Fort Worth Basin (Jarvie *et al.*, 2003, 2004b, 2005; Pollastro *et al.*, 2004a); and (4) inhibiting gas production from Barnett Shale where the Mineral Wells fault zone and associated fractures intersect Newark East field (Bowker, 2003; Pollastro, 2003).

A maximum thickness of sedimentary rocks in the Fort Worth Basin reach about 3660 m adjacent to the Muenster arch deposited over Precambrian granite and diorite

basement (Figure 2.3). The subsurface stratigraphic section of this basin composes of (1) 1220-1524 m of Ordovician – Mississippian carbonates and shales, (2) 1829-2134 m of Pennsylvanian clastics and carbonates, and (3) a thin Cretaceous rock, in the eastern part of the basin (Flawn *et al.*, 1961; Henry, 1982; Lahti and Huber, 1982; Thomson, 1988).

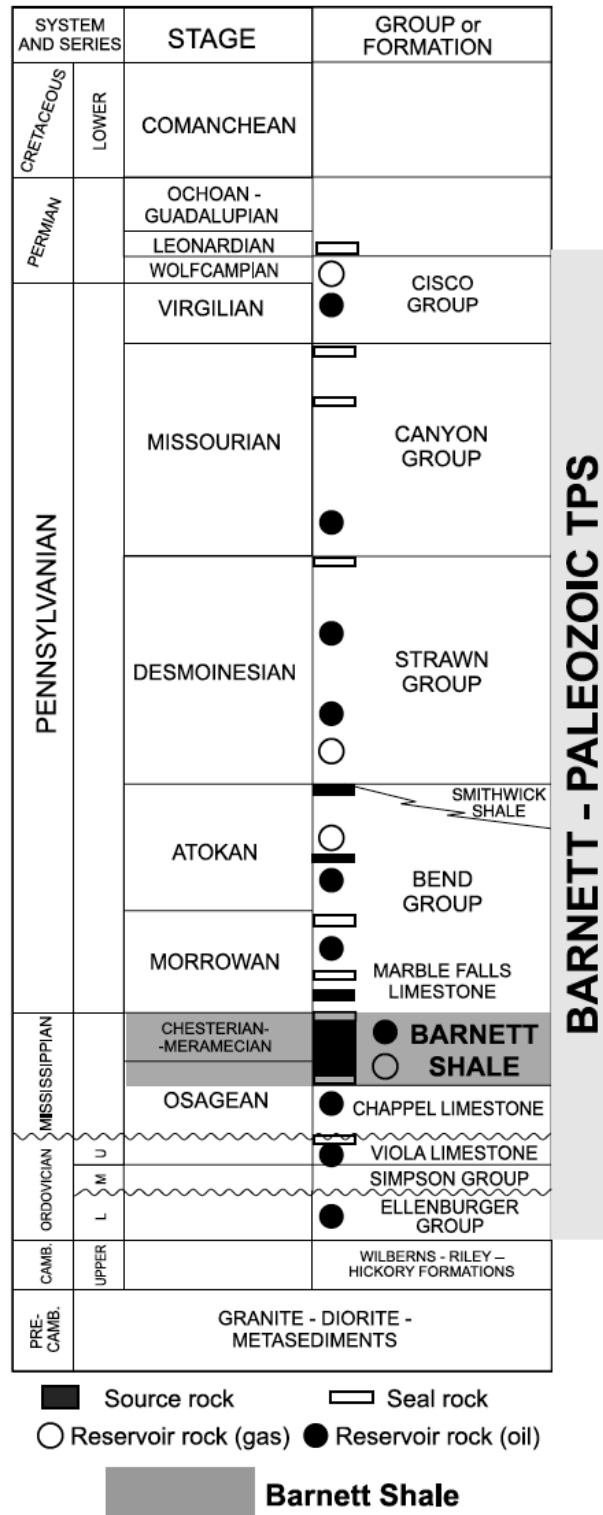
From the Cambrian to the Mississippian, this basin was a part of a stable cratonic shelf, with deposition dominated by carbonates (Turner, 1957; Burgess, 1976). Sloss (1976) and Kerans (1988) suggested that, during the Early Ordovician, the Ellenburger Group carbonate rock is interpreted as a broad epeiric carbonate platform covering all of Texas. At the end of Ellenburger deposition had a dropping sea level event resulting in platform exposure which brings about extensive karst feature in the upper part of the carbonate sequence. Henry (1982) also reported that there is a major erosion event, unconformity, removing any Silurian and Devonian rocks that may have been present in that area. After erosion event, there was a rising sea level event, in the Mississippian age, the shallow marine black Chappel Limestone and the organic-rich Barnett Shale had been depositing over most of the basin, respectively (Figure 2.3).

In the Pennsylvanian age, the Marble Falls Limestone deposited over the Barnett Shale following with clastic and mixed carbonate rocks representing a range of westward-prograding fluvial-deltaic deposits (Cleaves, 1982; Thompson, 1988). Terrigenous clastics originated mainly from uplifts of the Muenster arch in the north and the Ouachita fold and thrust belt in the east.

Permian rocks have been found in some parts of the Fort Worth Basin, but there is neither Triassic nor Jurassic rocks have been identified, maybe because of erosion event in pre-Cretaceous.

2.2 Barnett Shale deposition

The Barnett Shale spreadly slowly deposited under reducing conditions over a large part of north-central Texas during the late Mississippian on a shelf in the Fort Worth Basin (Figure 2.5) (Mapel *et al.*, 1979). The eastward thickening of the Barnett Shale (Figure 2.4) can interpret a source to east or northeast. The Hardeman Basin, the northern most basin of the Fort Worth Basin, presents the Barnett Shale which is an oil – prone Barnett Shale petroleum system (Pollastro *et al.*, 2004a, b). And the Midland, Delaware, and Polo Duro basins in the west also present the Barnett Shale. But along the Eastern shelf, the Barnett Shale is generally absent due to erosion and facies change into limestone to the northwest along the Chappel Shelf (Figure 2.5). Figure 2.4 updated from Pollastro (2003) shows a isopach map of the total Barnett Shale in the Bend arch - Fort Worth Basin. The Red River and Muenster arches and the Ouachita trust front control the geographic extent of this formation (Figure 2.1). Based on well-log interpretations of Figure 2.6, the thickness of the Barnett Shale is showed in constructed stratigraphic cross sections (Figure 2.7, 2.8). In the northern part of the basin, the thickness of Barnett Shale averages about 76 m whereas the thickest part is more than 305 m in the deepest part of the basin adjacent to the Muenster arch (Figure 2.4), where it is interbedded with limestone units which have a cumulative thickness of as much as 122 m (Mapel *et al.*, 1979; Henry, 1982; Bowker, 2003; Pollastro, 2003; Texas Railroad Commission, 2003). These limestones thin dramatically to the south and west away from the Muenster arch (Figure 2.9). The Barnett Shale rapidly thins to the west to only a few 3 m over the Mississippian Chappel shelf and along the Llano uplift (Figure 2.4, 2.8). Pollastro *et al.*, 2007 concluded that the Barnett Shale is absent in areas (1) where eroded along the Red River arch and Muenster arches to the north and northeast; (2) along the Llano uplift to the south; and (3) to the west, where there are an erosional limit and facies change to limestone.



BARNETT - PALEOZOIC TPS

Figure 2.3 Generalized subsurface stratigraphic section of the Bend arch – Fort Worth Basin province showing distribution of source rocks, reservoir rocks, and seal rocks of the Barnett-Paleozoic total petroleum system (Pollastro *et al.*, 2007).

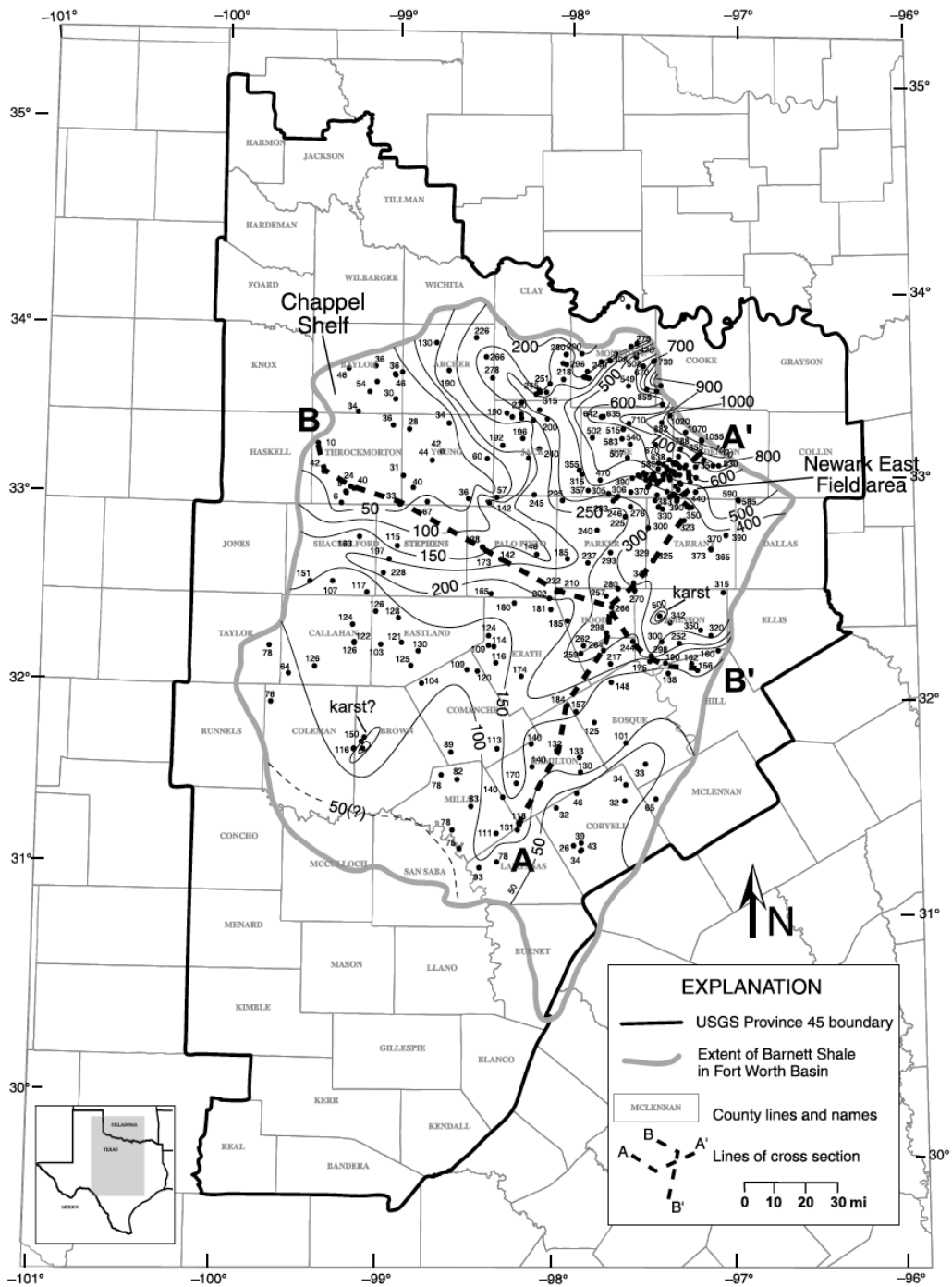


Figure 2.4 Map showing regional extent of Barnett Shale, thickness of Barnett Shale, isopachs of Barnett Shale, and lines of well-log cross sections AA' of Figure 2.7 and BB' of Figure 2.8. Contour intervals are 50 ft (15 m) for thicknesses from 0 to 300 ft (0 to 91 m) and 100 ft (30 m) for thicknesses from 300 to 1000 ft (91 to 305 m) (Pollastro *et al.*, 2007).

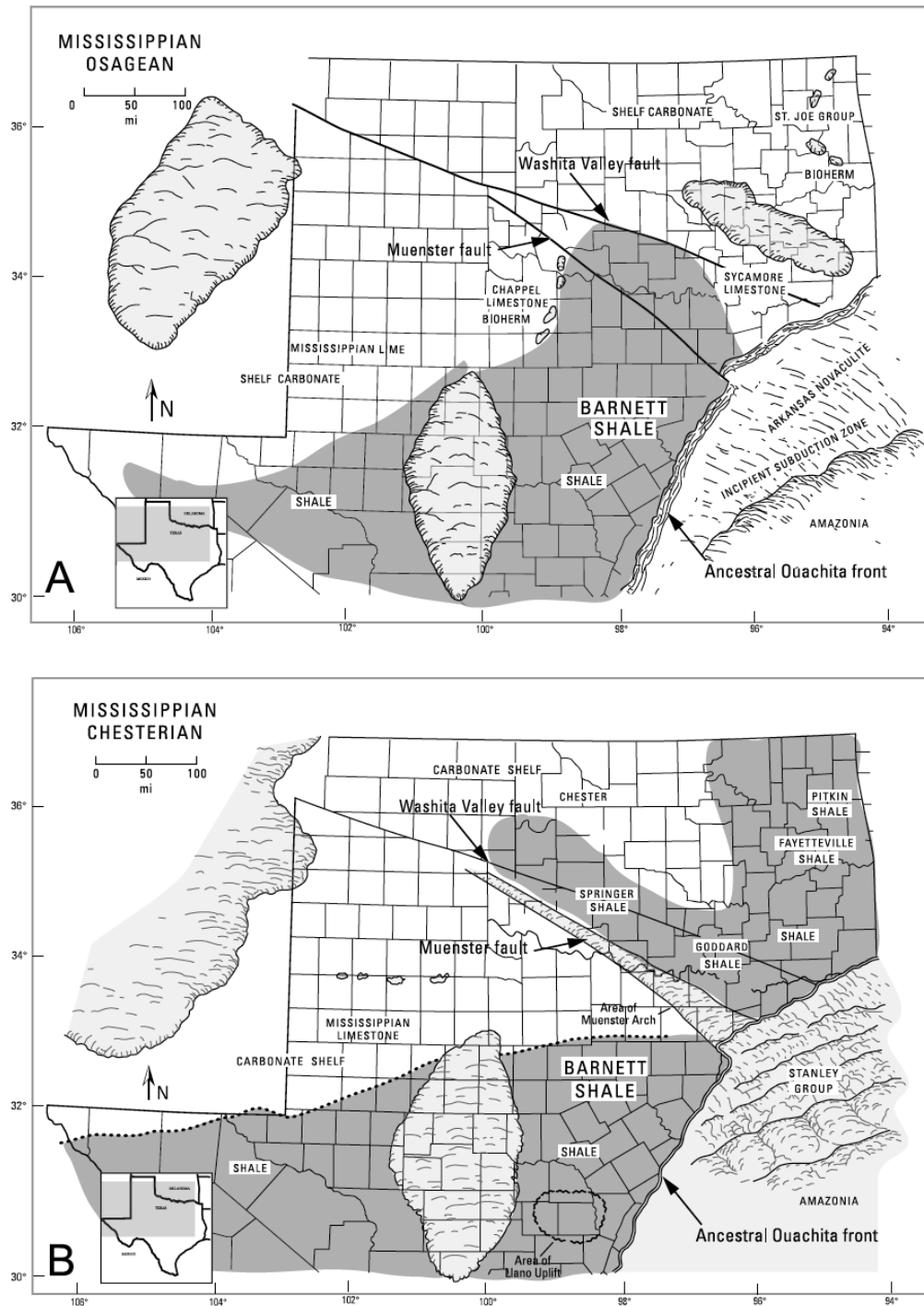


Figure 2.5 Paleogeographic maps of north Texas and southwestern Oklahoma during the Mississippian. (A) The Osagean showing incipient subduction zone and consequent uplift adjacent to present-day Fort Worth Basin and areas of deposition of the lower part of the Barnett Shale (dark shading), position of the Chappel shelf and bioherm deposition. Emergent areas are lightly shaded. (B) The Chesterian showing major structural features and area of upper Barnett Shale, or equivalent, deposition (dark shading). Emergent areas are light shaded (Pollastro *et al.*, 2007).

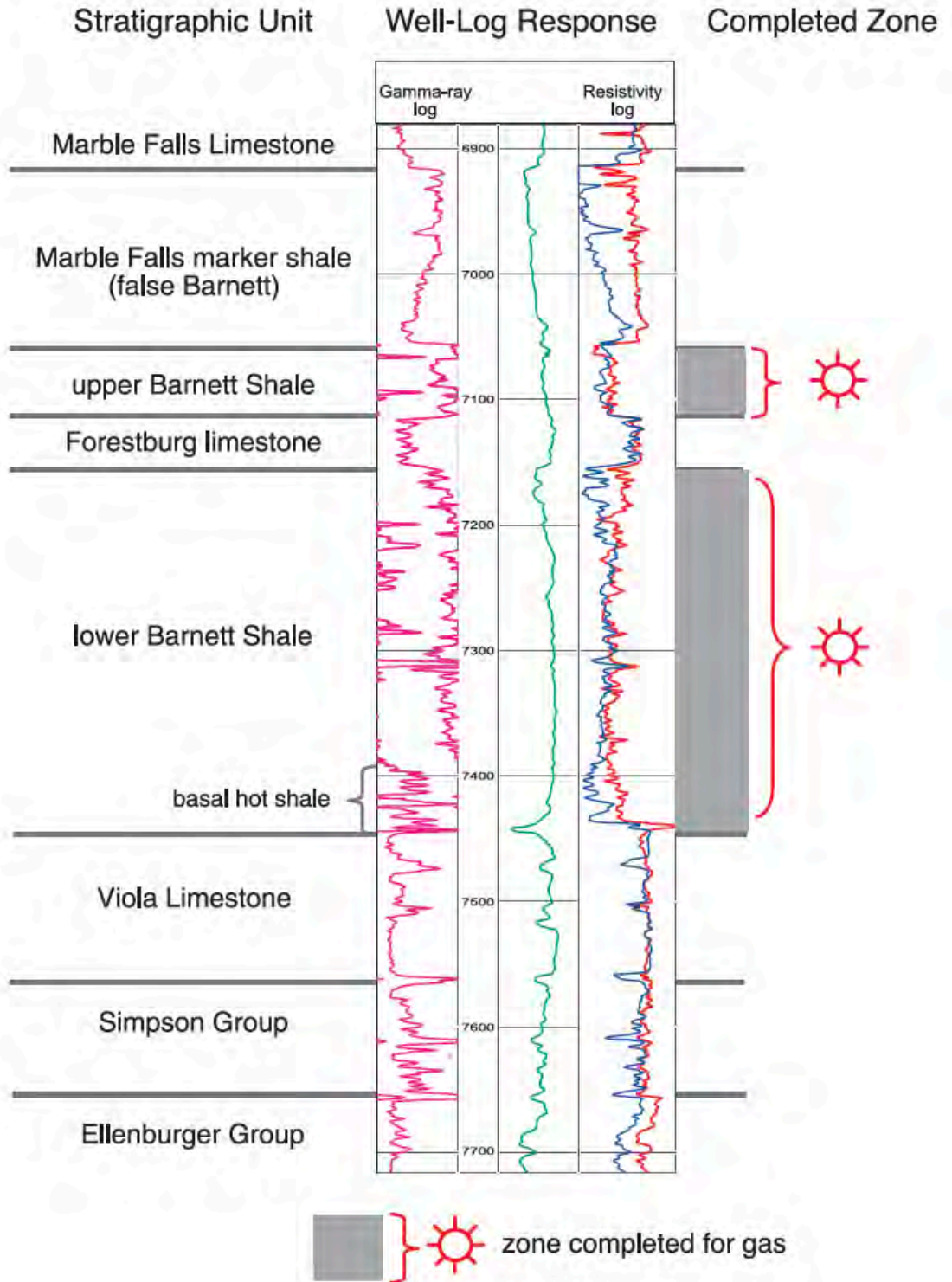


Figure 2.6 Typical well-log stratigraphic section showing gamma-ray and resistivity logs through the Barnett Shale and overlying and underlying units. Depth in feet (Pollastro *et al.*, 2007).

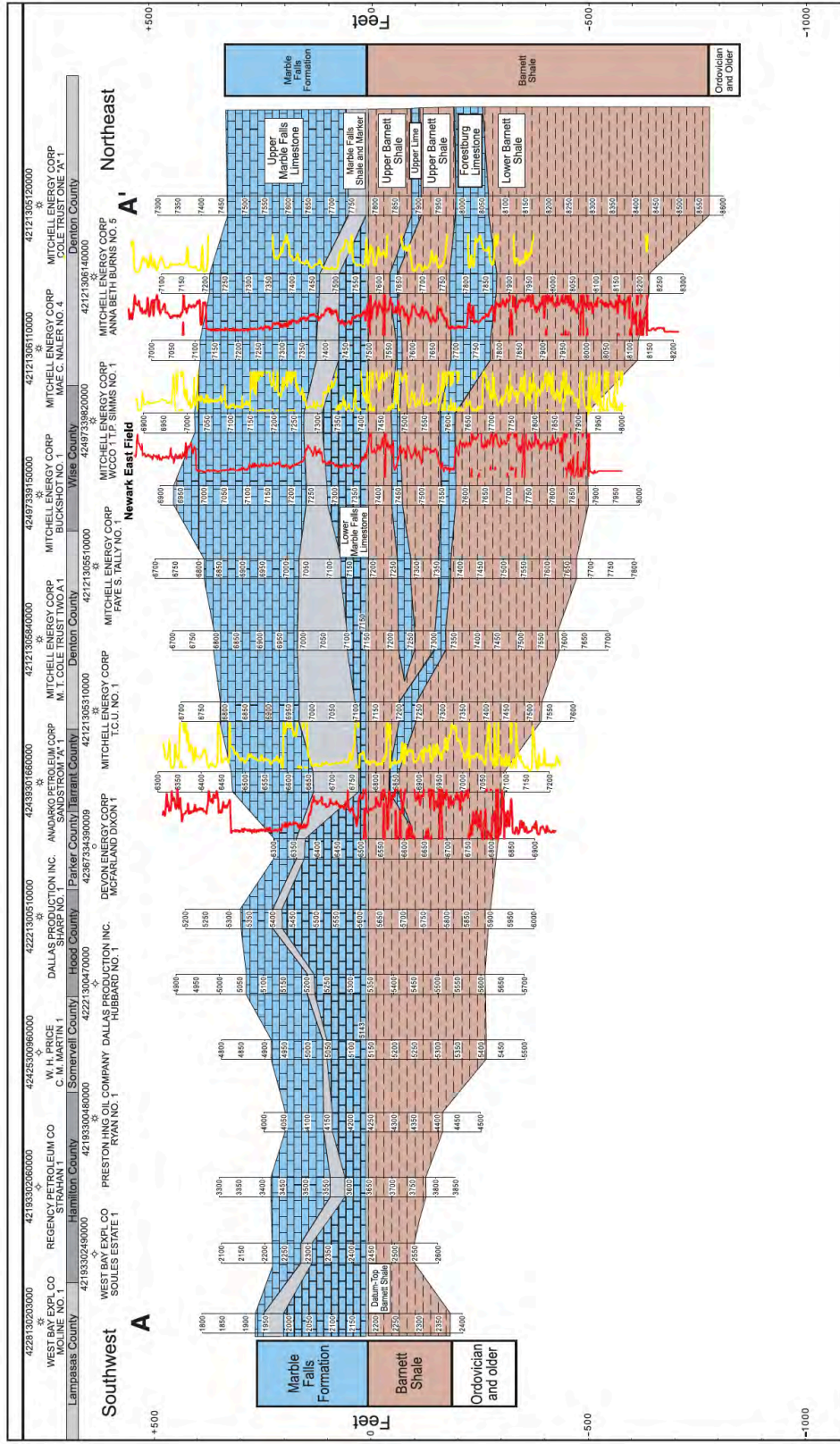


Figure 2.7 Generalized southwest-northeast stratigraphic cross section AA' based on well-log correlations; line of section is from Figure 2.4. Gamma-log profile (red) and resistivity-log profile (yellow) are shown for reference on selected wells (Pollastro et al., 2007). Not to scale

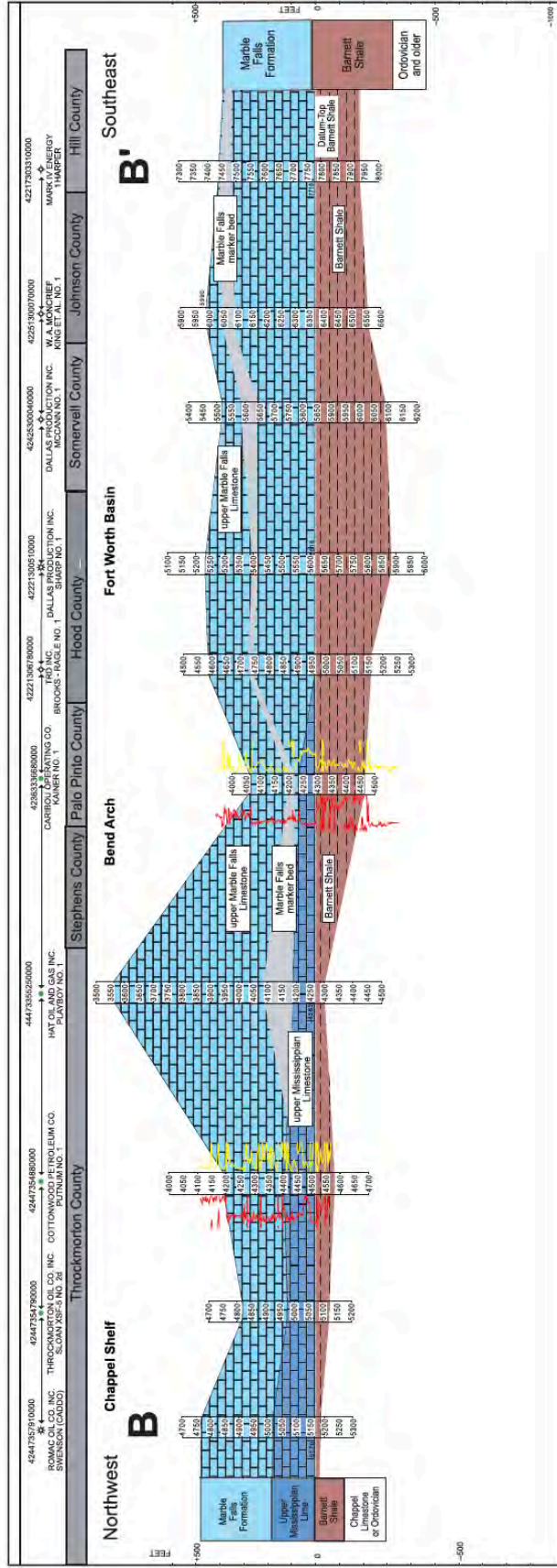


Figure 2.8 Generalized northeast-southwest stratigraphic cross section BB' based on well-log correlations; line of section is from Figure 2.4. Gamma-log profile (red) and resistivity-log profile (yellow) are shown for reference on selected wells (Pollastro et al., 2007). Not to scale horizontally.

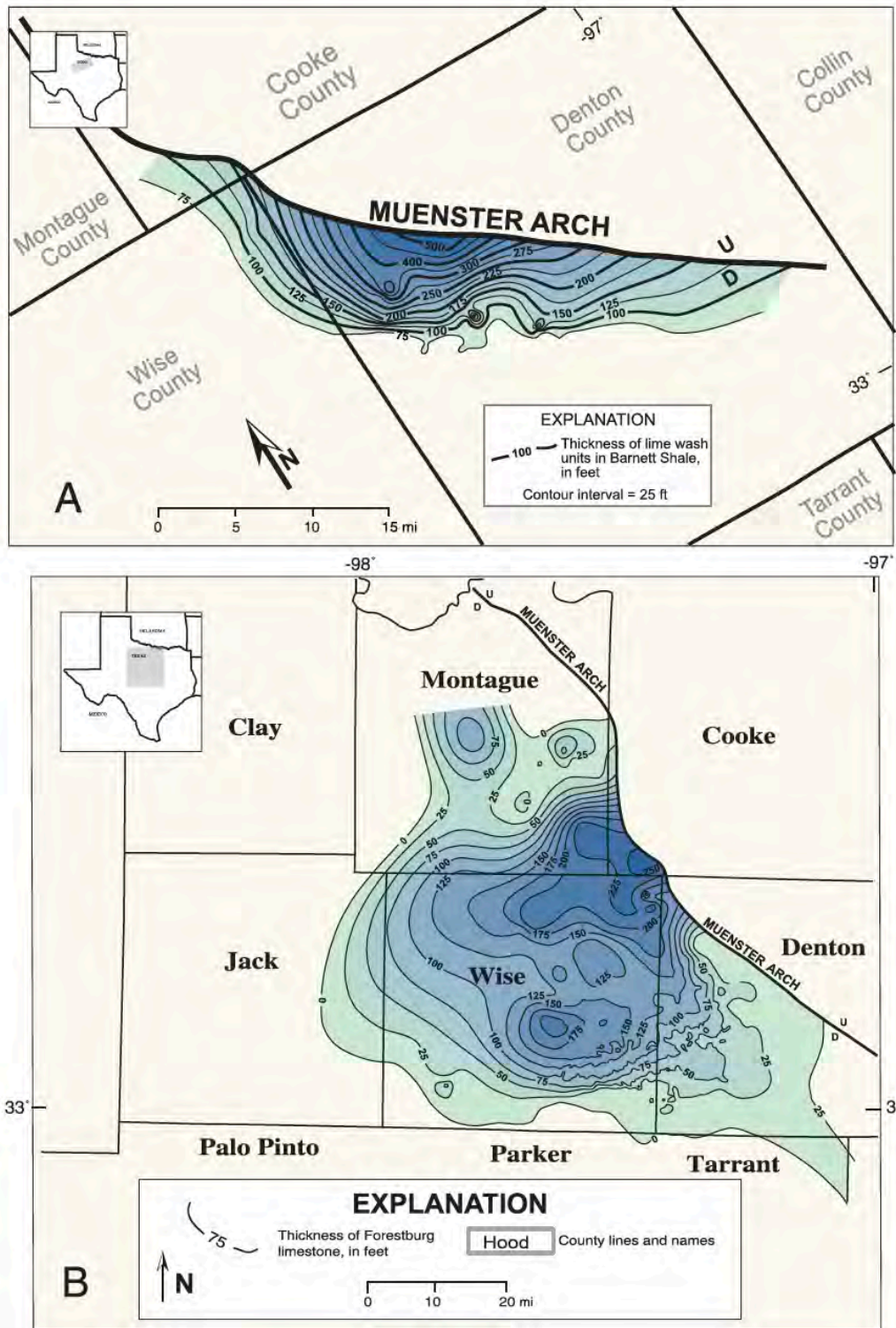


Figure 2.9 Isopach maps of limestone units in Barnett Shale. (A) Lime wash units within the Barnett Shale, Fort Worth Basin, Texas. Contour interval equals 25 ft (8 m). (B) Forestburg limestone within the Barnett Shale, Fort Worth Basin, Texas. Contour interval equals 25 ft (8 m) (Pollastro *et al.*, 2007).

In Newark East field area, the Barnett Shale is informally into lower and upper formations which are separated by a carbonate rock unit known as the 'Forestburg limestone' (Henry, 1982) (Figure 2.6, 2.7). In the area adjacent to the Muenster arch, there is the thickest part of the Forestburg Limestone exceeding 61 m, but thins rapidly to absent to south- and westward of the field (Figure 2.7, 2.9B), whereas the upper Barnett Shale can be found farther westward (Figure 2.7, 2.10). Where the Forestburg limestone is absent, upper and lower Barnett Shale are undifferentiated on well logs and maps (Figure 2.7).

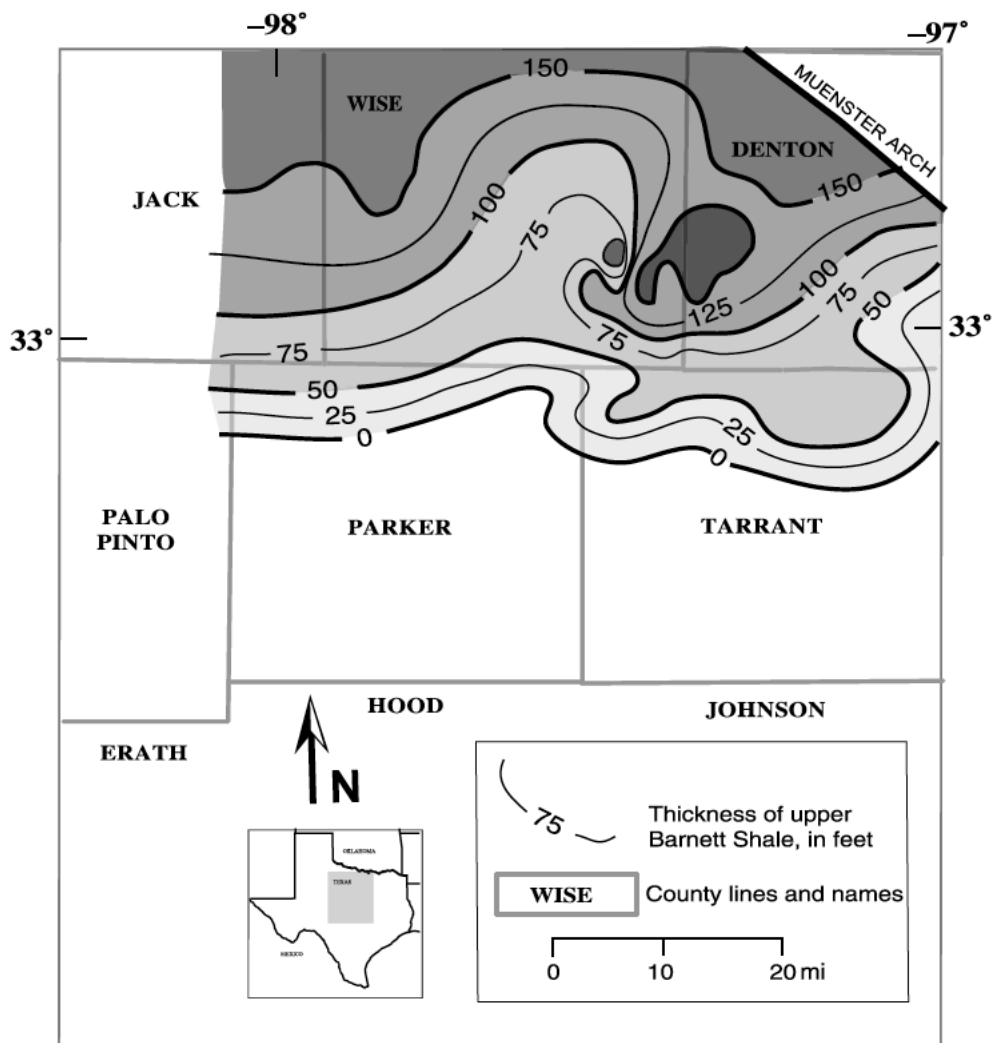


Figure 2.10 Isopach map of the upper Barnett Shale unit, Fort Worth Basin, Texas (Pollastro *et al.*, 2007).

2.3 Petroleum geochemistry and Thermal history of Barnett Shale

Oil and gas produced from Bend arch – Fort Worth Basin were generated mostly from the Barnett Shale (Pollastro *et al.*, 2007). Figure 2.2A shows mean TOC values of Barnett Shale which are averaged from multiple well and cutting samples taken at various depths ranging about 3-5 wt.% and consisted mostly of oil-prone type II kerogen. Vertical movement along the fault systems in the basin and any associated high heat flow could have caused thickening or thinning of the Barnett Shale section and elevated mean R_o (Figure 2.11), respectively, along this east-west trend.

Secondary significant potential source rocks in the Bend arch – Fort Worth Basin are from organic – rich carbonate rocks and shales in the Pennsylvanian age (Figure 2.3, 2.13). Oil and associated gas were initially generated from the decomposition of kerogen at moderate thermal maturities ($R_o = 0.6-1.1\%$), whereas non-associated gas in the Newark East field area are formed at higher thermal maturities ($R_o > 1.1\%$) (Figure 2.12). Variable thermal maturities, as determined from vitrinite reflectance measurements, indicate that heat-flow regimes possibly emanating from the Ouachita thrust front and the Mineral Wells – Newark East fault system and migrating along fault systems, locally influenced the thermal history of the Barnett Shale.

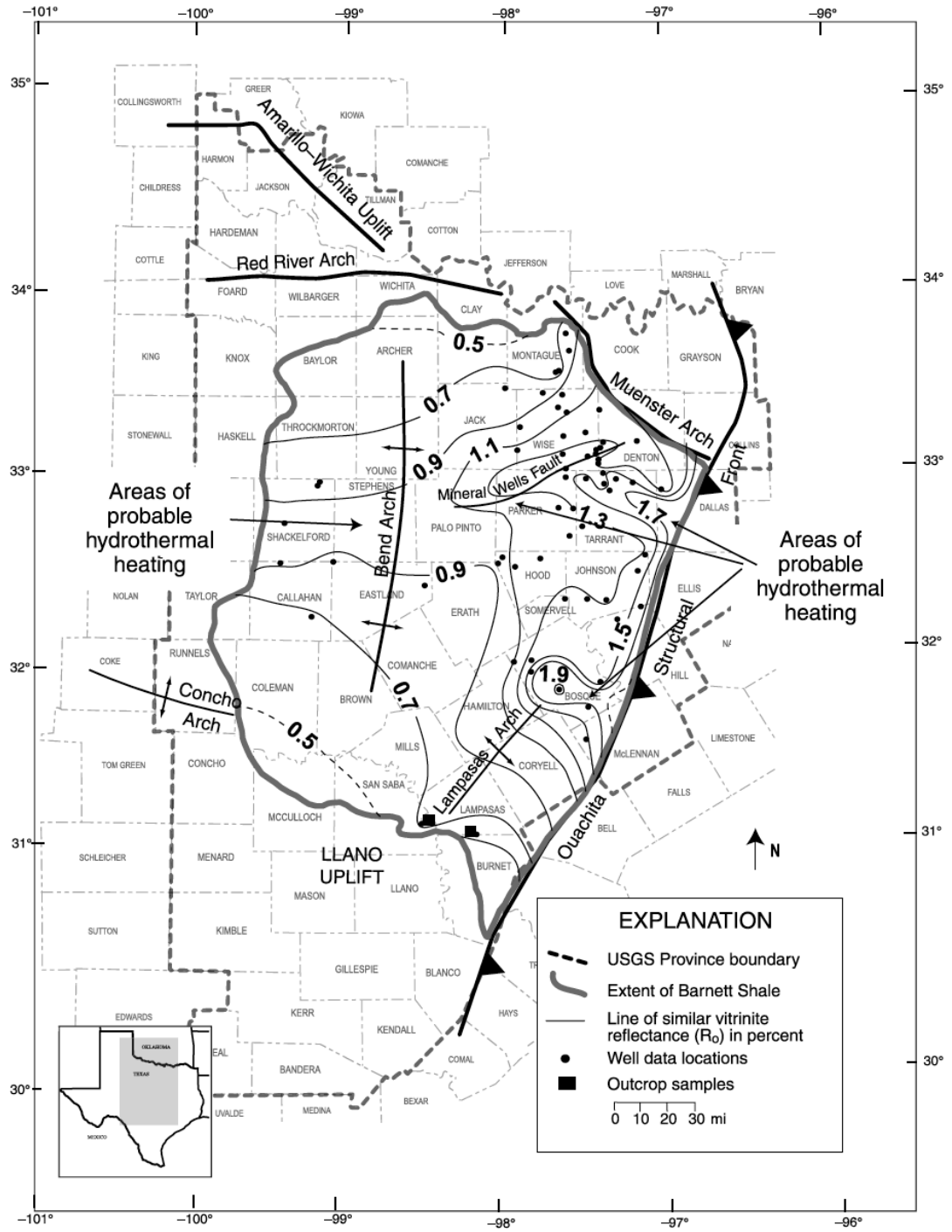


Figure 2.11 shows lines of equal thermal maturity map as determined from mean vitrinite reflectance (R_0) of Barnett Shale. Areas of probable high hydrothermal heating and anomalously high R_0 are also indicated (arrows) (Pollastro *et al.*, 2007).

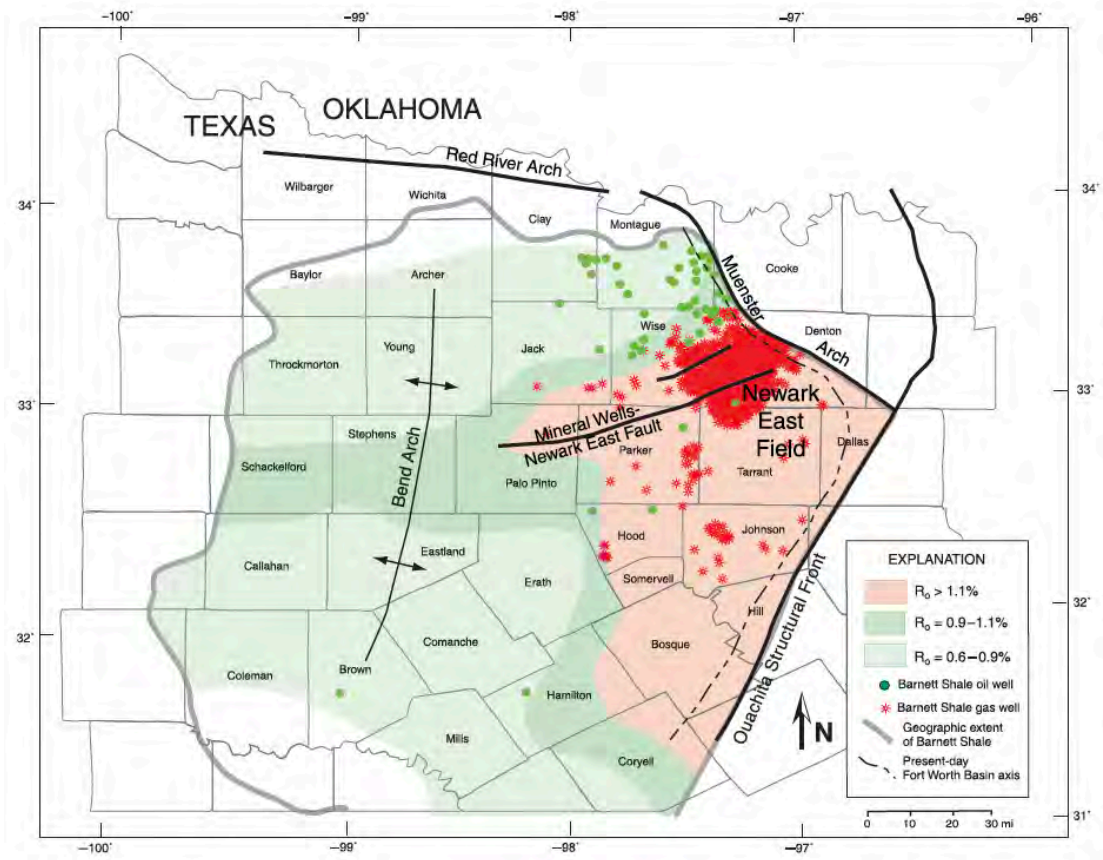


Figure 2.12 shows relation between oil and gas production from Barnett Shale in Fort Worth Basin versus oil- and gas-generation windows as determined from mean vitrinite reflectance (R_o) (See Figure 2.11) (Pollastro *et al.*, 2007).

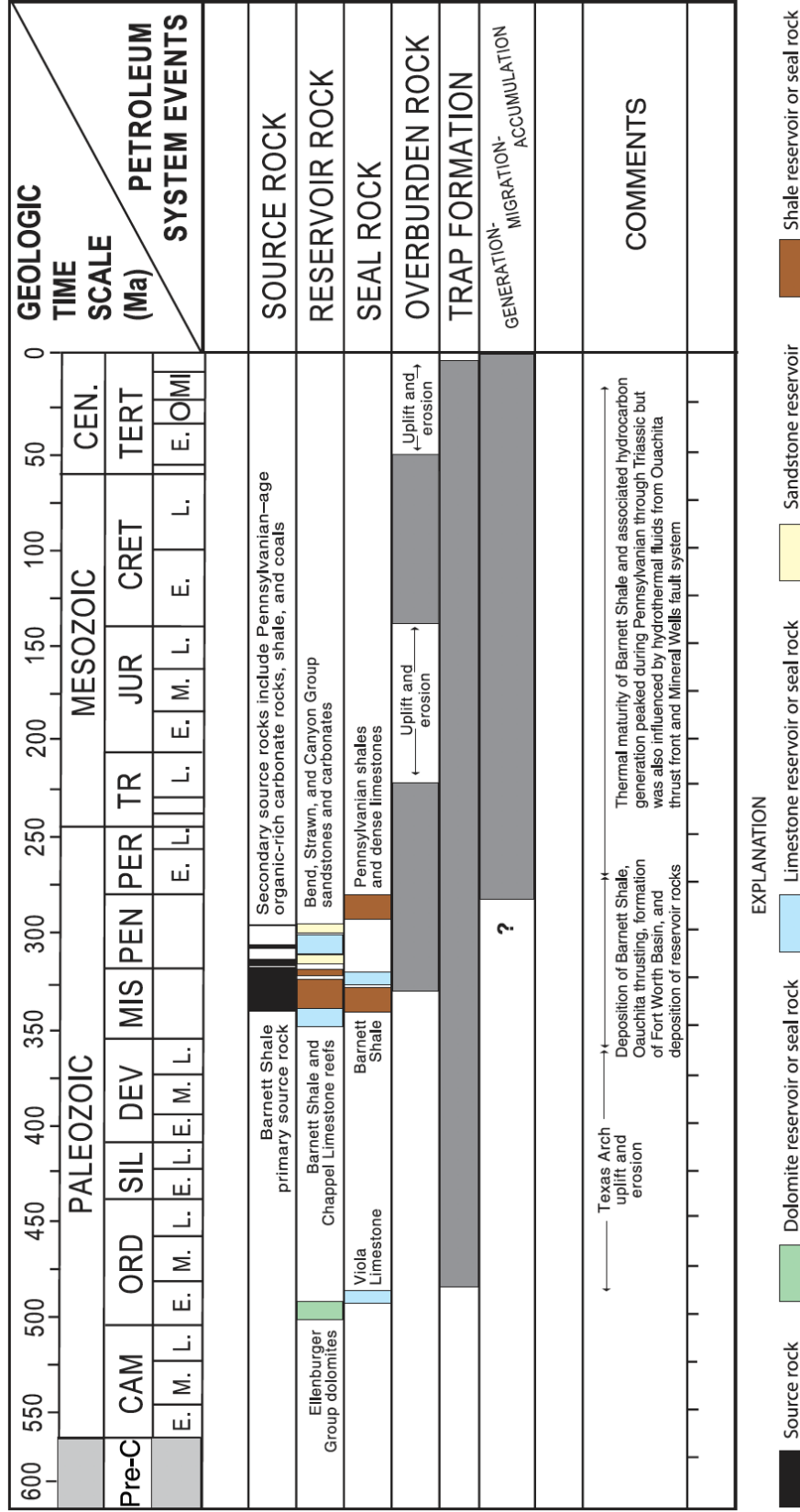


Figure 2.13 Petroleum system events chart for Barnett-Paleozoic total petroleum system of the Fort Worth Basin. Abbreviations: E = early; M = middle; L = late; Cam = Cambrian; Ord = Ordovician; Sil = Silurian; Dev = Devonian; Mis = Mississippian; Pen = Pennsylvanian; Per = Permian; Tr = Triassic; Jur = Jurassic; Cret = Cretaceous; Ter = Tertiary; Cen = Cenozoic; O = Oligocene; Mi = Miocene (Pollastro *et al.*, 2007).

EXPLANATION

- Source rock
- Dolomite reservoir or seal rock
- Limestone reservoir or seal rock
- Sandstone reservoir
- Shale reservoir or seal rock

CHAPTER III

METHODOLOGY

In this study are separated into 2 phases; (1) Laboratory phase, and (2) Data analysis phase. In the laboratory phase, The Deformation-DIA (D-DIA) apparatus is used to increase pressure and temperature to the sample reaching over 200 Ma, 100 °C. Moreover, Synchrotron X-ray Micro-tomography (SYN-MCT) and Synchrotron X-ray Diffraction (SYN-XRD) techniques are used in this study so as to correct the data for data analysis phase. In the data analysis phase, Material Analysis using Diffraction (MAUD) is used to investigate; (1) mineral compositions, (2) preferred orientation, and (3) elastic property of composed minerals. Furthermore, segmentation program had been used to reconstruct 3D images of studied rock for; (1) investigate distribution of pore and kerogen (before compression), and fracture (after compression), and (2) calculate volumes of those pores, kerogen, and fractures.

3.1 Laboratory phase

3.2.1. Sample preparation

Once we corrected the sample from conventional core from the Barnett Shale, we prepared it following these steps.

(1) sharpened in cylindrical shape with 4 mm for diameter and 4 mm for axis.

(2) contained sample by placing its bedding plane in horizontal direction into Pressure Transmitting Medium. In this case, Pressure Transmitting Medium is cubic shape made from alloy materials. The reasons we used Pressure-transmitting Medium are for (1) gently increasing pressure from anvils to sample, and (2) protecting collision of those anvils.

3.2.2. Before compression

Once the sample was contained in Pressure-transmitting Medium. We used SYN-MCT to investigate distribution and quantity of pores, kerogen and fractures.

3.2.3. During compression

This study is *in situ* experiment started from ambient condition (Time period 001). Then, it was increased temperature and pressure for simulating the subsurface condition (Start at time period 002). During the compression, SYN-XRD was used for collecting diffraction images and radiographic images. In some cases, anvils were released to investigate elastic property of minerals and fractures development of this sample (Table 3.1). In data analysis phase, the diffraction images in these steps were used in MAUD and the radiographic images were used for strain calculation.

Time periods	Temperature (°C)	Pressure (ton)	Anvils status
001	25	0	-
002	100	11	Compress with hydrostatic stress
003	100	11	Compress with uniaxial stress
004	100	11	Compress with uniaxial stress
005	100	11	Compress with uniaxial stress
006	100	11	Release anvils
007	100	11	Release anvils
008	100	11	Compress with uniaxial stress
009	100	4	Release anvils
010	100	0	Release anvils

Table 3.1 shows state conditions and anvils status of the samples

3.2.4. After compression

The SYN-MCT was used again to investigate distribution and quantity of pores, kerogen, and fractures.

3.2 Data analysis phase

3.2.1. Material Analysis Using Diffraction (MAUD)

Once we got 10 diffraction images from laboratory phase, we had to centralize those images one by one via ImageJ by

- (1) *Change Image Properties*. Use these parameters; Unit of length in mm, Pixel width 0.079, Pixel height 0.079, and Voxel depth 0.079 (Figure 3.1).

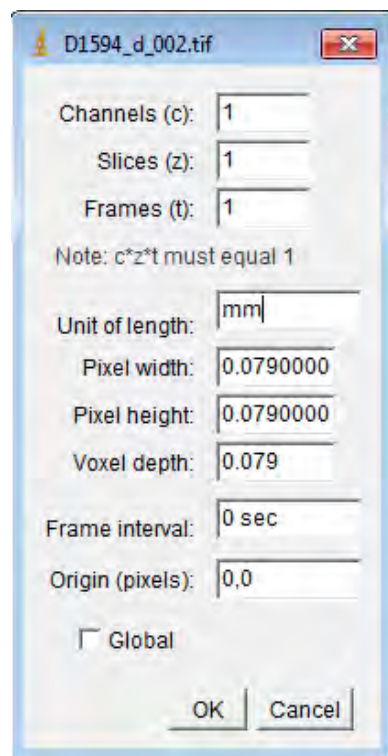


Figure 3.1 shows values of parameters in image properties.

- (2) *Transform image*. Rotate images 90° counter-clockwise.
- (3) *Centralize and Integrate Debye-Scherrer Rings*. Drag a Square, Select Multi-Spectra from normal

transmission/reflection image in Plugins, MAUD Plugins. Then, Choose the integration lines. In this study use these parameters; Sample – Detector distance (mm) 414, Center X (mm) 80.92, Center Y (mm) 81.06, Tracker circle radius (deg 2Theta) 50, Start Angle (in deg) 0, Final Angle (in deg) 360, Number of Spectra 36, Omega angle (in deg) 0, Chi angle (in deg) 0, and Phi angle (in deg) 0. Then, export esg files (Figure 3.2).

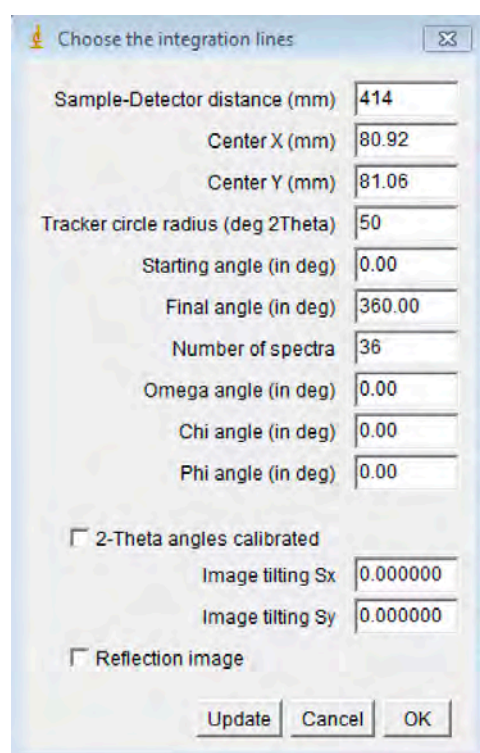


Figure 3.2 shows values of parameters in Centralize and Intergrate Debye-Scherrer Rings.

The refinement of their parameters in MAUD based on Rietveld refinement is quite complex due to their texture of composed minerals and stresses. We need to refine those parameters one by one following these steps. We try as much as possible to avoid refining unnecessary parameters.

- (1) *Import esg file.* Start with time period 001. Then, remove 18 integrated angle because it lacks data (Figure 3.3).

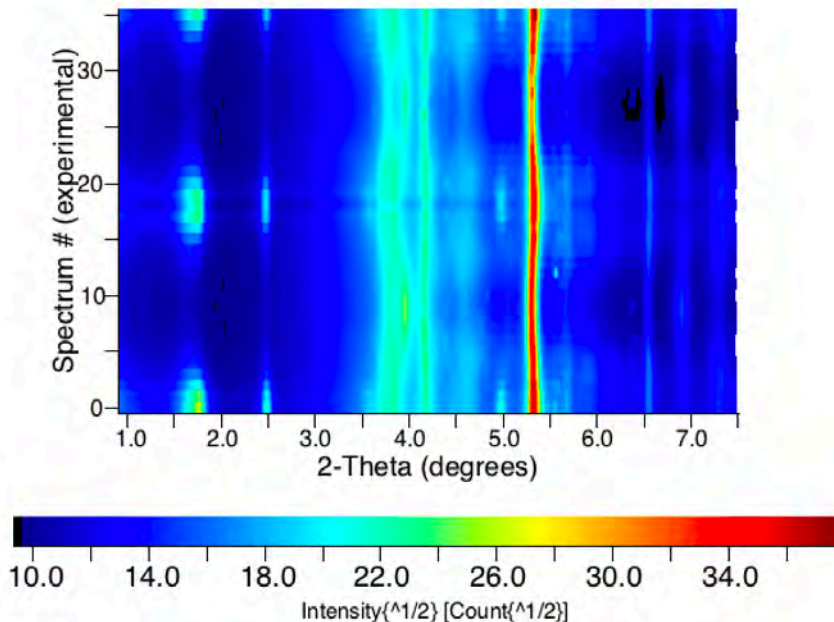


Figure 3.3 shows plot 2D of time period 001 lacking data in 18 integrated angle.

- (2) *Select Computation range.* In this study is investigated from 0.9 to 7.5 (Figure 3.4).

Computation range	
Min in data units:	0.9
Max in data units:	7.5
Data in groups of:	1

Figure 3.4 shows Computation range.

- (3) *Import quartz CIF file.* In order that refinement in the next step.
- (4) *Diffraction Instrument.* In this calibration, there are many parameters need to refine: (1) Intensity Calibration choose none cal. (2) Angular calibration choose Flat Image Transmission. Starting with 414 mm for Detector Distance.

Then, refine this parameter. Fix the rests. (3) Geometry select Image 2D. (4) Measurement choose 2Theta. (5) Source is from Synchrotron with 0.309950 Angstrom for Wavelength and 1.0 for Weigth. Fix both. (6) Detector is Scintillation. And (7) Instrument Broadening select Caglioti PV. Then launch refinement. After that, refine center X error and center Y error in Angular calibration (Flat Image Transmission). Launch refinement. Following with refine tilting error X and tilting error Y. Launch refinement. End with fix all parameters in this calibration. Export this instrumental file. All time periods are used the same (this) instrumental calibration (Figure 3.5, 3.6, 3.7).

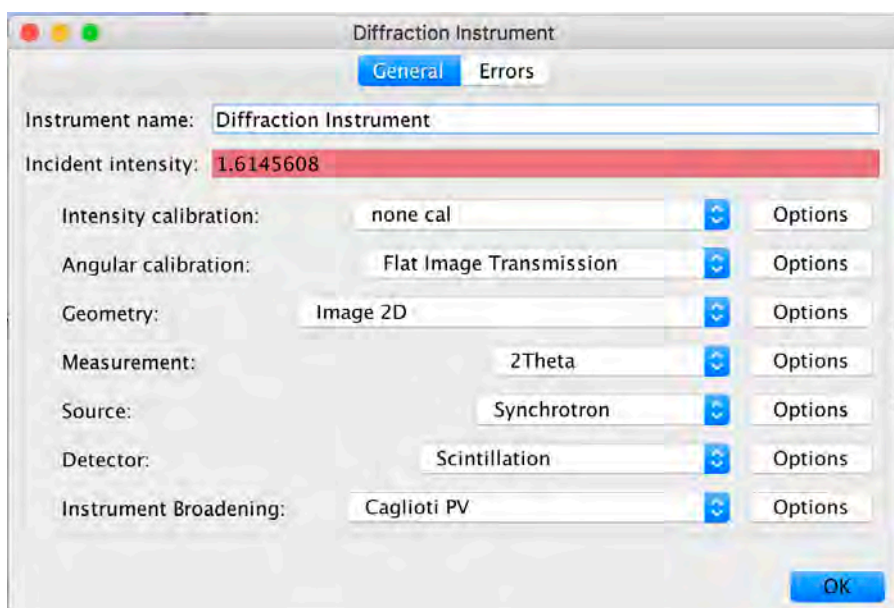


Figure 3.5 shows parameters in Diffraction Instrument.

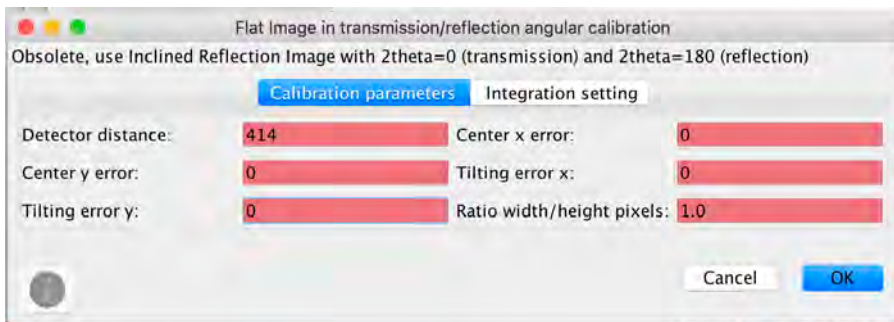


Figure 3.6 shows parameters in Flat Image in transmission/reflection angular calibration.

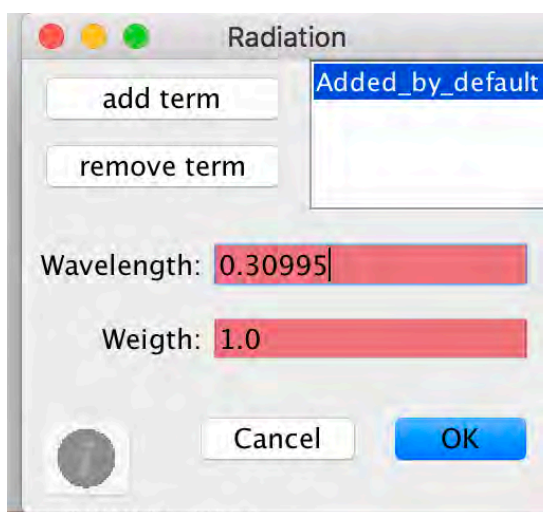


Figure 3.7 shows parameters in Source from Synchrotron.

- (5) *Background peak fitting*. In this study, we add 3 terms following Background peak from 2D plot which are 0, 170 and 340 for Position (eta). And in Plot, the first highest peak of background is about 0.91 degrees put in Position. Fix those parameters. The refined parameters are (1) Height (100,000) (2) HWHW (0.05) (3) HWHM (eta) (40). Launch refinement. After they are almost perfectly fit, fix all parameters in this calibration (Figure 3.8, 3.9, 3.10).

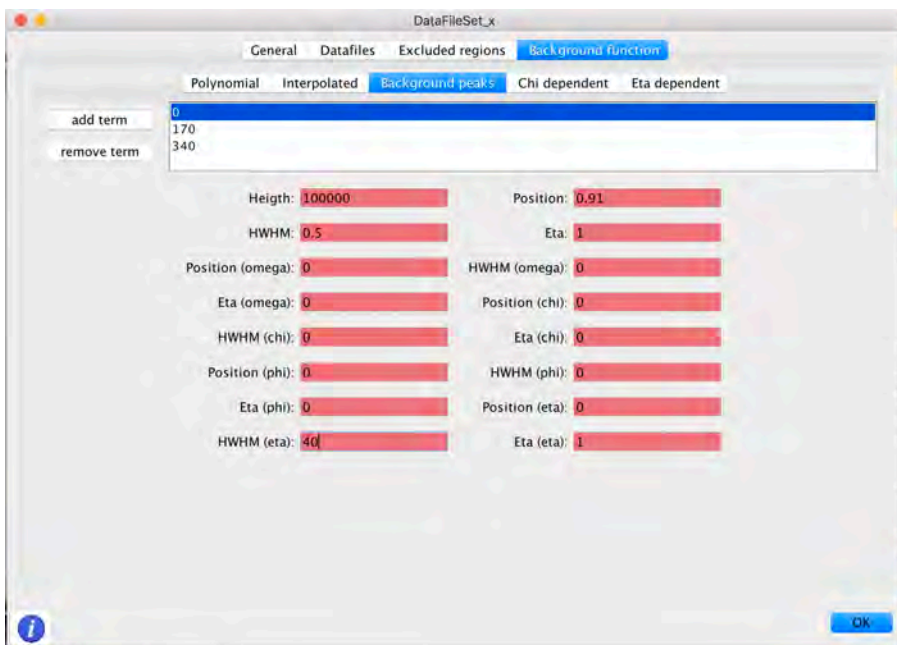


Figure 3.8 shows parameters in Background peaks at position 0 eta.

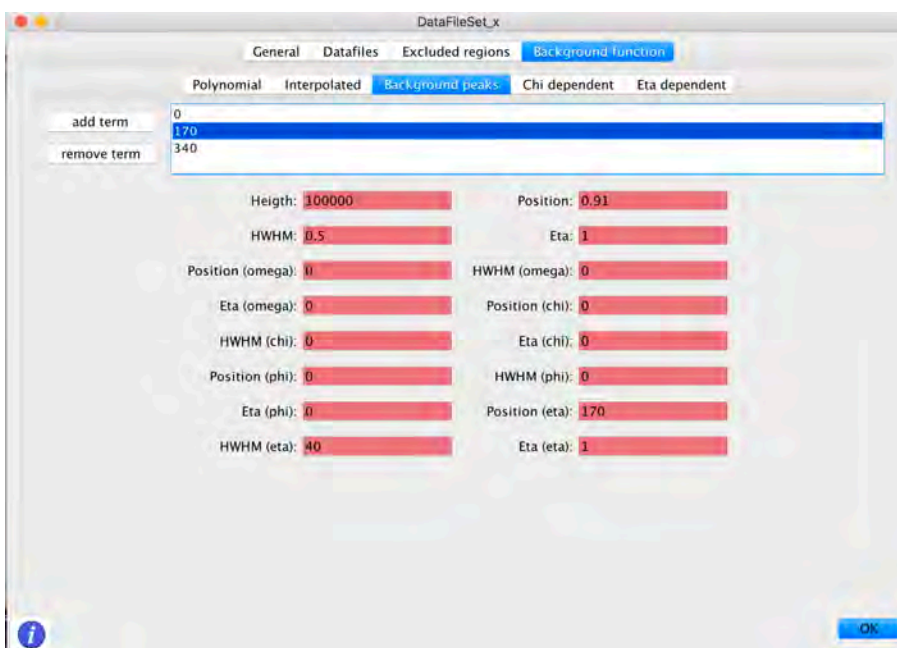


Figure 3.9 shows parameters in Background peaks at position 170 eta.



Figure 3.10 shows parameters in Background peaks at position 340 eta.

(6) *Import the rest mineral CIF files.* In this study, there are illite-mica, illite-smectite, kaolinite, and pyrite. We know because of their highest peak from Plot graph. In this study, we have to change space group of illite-mica to be C2/C:C1. In addition, Pressure Transmitting Medium also effects to the diffraction image. So, we have to simulate CIF file of this material (Figure 3.11, 3.12).

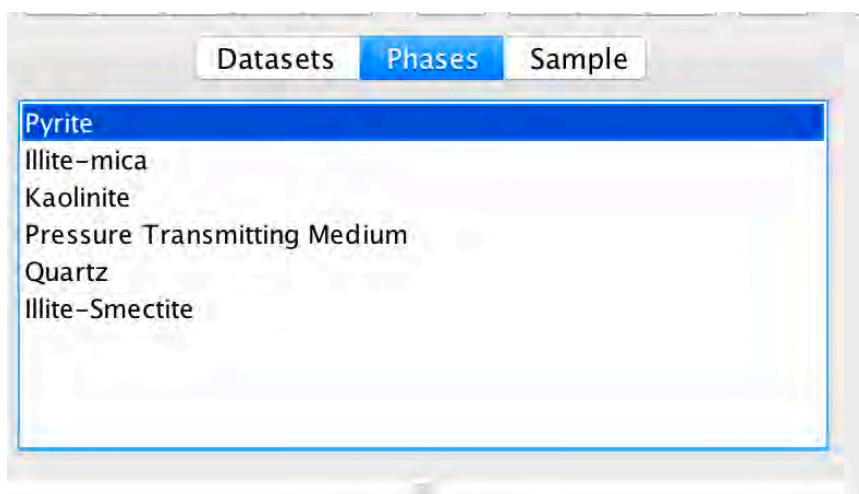


Figure 3.11 shows mineral and Pressure Transmitting Medium CIF files used in this study.

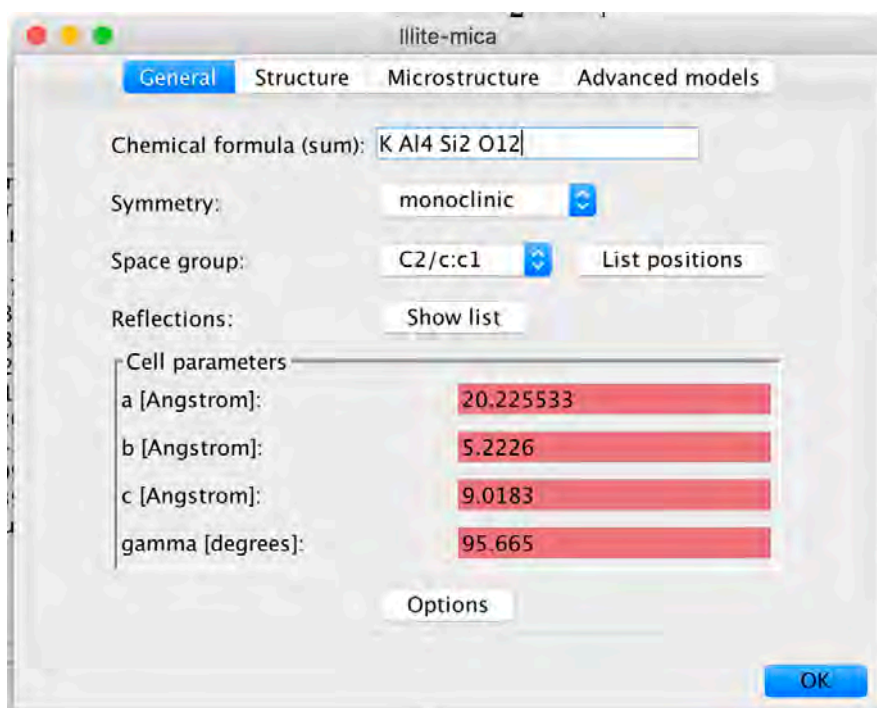


Figure 3.12 shows changed space group of illite-mica.

- (7) *Cell Parameter*. First of all, we have to set Biso factor at 1. Then, Free scale pars and Bound B factors. After that, refine cell parameters of those phases by illite-mica, illite-smectite, and pyrite are refined only a , kaolinite is refined only c , and quartz is refined a and c . These refinements bring

about to shift of the peaks. After those peaks place on right position. We will refine Microstructure. Then, (1) assume that these minerals Size-Strain model of minerals are Isotropic (2) set Crystallite size (A) and R.m.s. microstrain following these values: illite-mica (500, 0.001), illite-smectite (300, 0.01), kaolinite (500, 0.001), quartz and pyrite (1000, 6.0E-4). Then, launch refinement. After they are perfectly fit, fix all parameters.

- (8) *Stress model*. The Sinusoidal variations in peak position with azimuthal angles are due to elastic strain in response to differential stress which is defined as t . And differential or deviatoric (D_{ij}) components are defined as;

$$D_{ij} = \begin{bmatrix} -t/3 & 0 & 0 \\ 0 & -t/3 & 0 \\ 0 & 0 & 2t/3 \end{bmatrix}$$

In this study, Moment pole stress model (Matthies *et al.*, 2001; Wenk *et al.*, 2014) is used to investigate differential components (macrostresses) from variations in peak position by using the BulkPathGeo stress/strain averaging model (Matthies *et al.*, 2001) depending on their elastic coefficient or stiffness (C_{ij}) of minerals. Due to equation above, we refine only macrostress₁₁ and fix macrostress₂₂ equal to 1 time of macrostress₁₁ and macrostress₃₃ equal to -2 times of macrostress₁₁, the rest are zero. So, we can calculate t from macrostress₁₁. (For time period 001 skip this process because there is no stress/strain on these ones.) For C_{ij} of minerals using following these values (Table 3.2) (Vasin *et al.*, 2013; Heyliger *et al.*, 2003);

Stiffness (C_{ij})	illite-mica	illite-smectite	kaolinite	quartz
C_{11}	60.14	25.15	187.42	87.26
C_{12}	25.55	5.89	70.41	6.57
C_{13}	23.97	2.43	4.84	11.95
C_{14}	-	-	-	-17.18
C_{22}	184.36	170.58	179.70	87.26
C_{23}	52.93	27.87	5.89	11.95
C_{24}	-	-	-	17.18
C_{33}	170.00	188.50	83.91	105.8
C_{44}	70.42	60.34	13.52	57.15
C_{55}	18.48	5.46	16.04	57.15
C_{56}	-	-	-	-17.18
C_{66}	22.15	17.49	61.08	40.35

Table 3.2 shows stiffness of illite-mica, illite-smectite, kaolinite, and quartz.

(9) *Texture*. We use E-WIMV method for illite-mica, illite-smectite, and kaolinite because they are clay minerals following these parameters; Iterations number 10, Generate symmetry fiber, and ODF resolution in degrees 10. And quartz, we use arbitrary tex because there is no texture in this mineral (Figure 3.13).

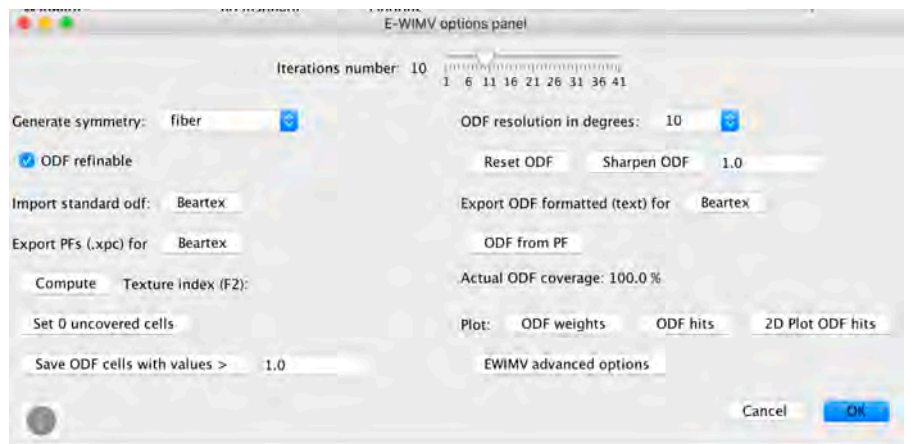


Figure 3.13 shows parameters in E-WIMV method for illite-mica, illite-smectite, and kaolinite.

3.2.2. Segmentation program

Once we got reconstructed images from SYN-MCT, before segmentation process we have to import those images into segmentation program.

3.2.2.1. Before compression's images

- (1) *Import images.* Before compression we have 1501 images starting with 0 to 1500. But there is only image number 300 to 1299 which have perfect data. So, we use only 1000 images.
- (2) *Set Voxel size.* The voxel size of this experiment is $0.72 \mu\text{m}$
- (3) *Crop studied area.* In this study, we crop studied area from 950 to 1549 in x axis, 950 to 1549 in y axis. So, the studied 3D image will be in the $600 \times 600 \times 1000$ voxels.
- (4) *Normalize Grayscale.* In this function will normalize color of image in to grayscale value from 0 to 255.
- (5) *Median Filter.* To reduce artifacts and noise by replacing the grayscale value of each voxel with a median of its neighborhood within $3 \times 3 \times 3$ voxel window.
- (6) *Segmentation Grayscale.* Different components segmented by the thresholding method by assigning a label to every voxel and effectively distinguishing between low- and high-absorbing phases. The highly absorbing particles (white) are pyrite. While the low-absorbing feature (dark gray) represent low-density which is kerogen. The lowest-absorbing phases (black) are pore and fractures.
- (7) *Dilation.* This function dilates segmented features in all direction so as to make it connect each other.
- (8) *Erosion.* Once it is connected, we have to erode those segmented features which are not connected each other to normalize them into the right size.

(9) *Axis Connectivity*. This function will calculate connectivity of feature especially pore and fractures to determine permeability in x, y, and z axis in the next step. But before compression's data, there is no output in this step that means there is no connectivity all of those directions.

3.2.2.2. After compression's images

- (1) *Import images*. After compression we have 888 images starting with 0 to 887. But there is only image number 171 to 710 which have perfect data. So, we use only 540 images.
- (2) *Set Voxel size*. The voxel size of this experiment is 0.69 μm
- (3) *Crop studied area*. In this study, we crop studied area from 801 to 1600 in x axis, 801 to 1600 in y axis. So, the studied 3D image will be in the 800 x 800 x 540 voxels.
- (4) *Normalize Grayscale*.
- (5) *Median Filter*.
- (6) *Segmentation Grayscale*.
- (7) *Dilation*.
- (8) *Erosion*.
- (9) *Axis Connectivity*. There are output only in x and y directions.
- (10) *Absolute Permeability Experiment Simulation*. Using for calculating permeability and generating streamlines. In this study, we input these parameters; input pressure 130000 Pa, output pressure 100000 Pa, and Fluid Viscosity 0.001 Pa.s.

CHAPTER IV

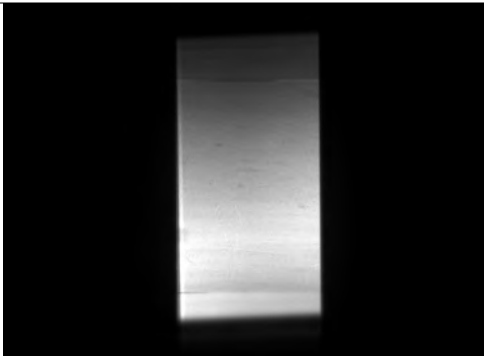
RESULTS

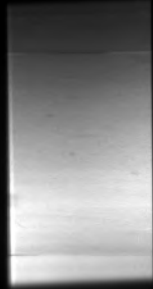
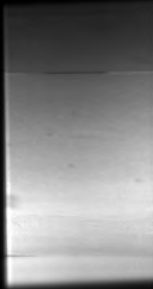


This study is investigated mineral composition, preferred orientation and elastic property of constituent minerals using Synchrotron X-ray Diffraction (SYN-XRD) analyzed by Material Analysis Using Diffraction (MAUD) based on the Rietveld refinement. Moreover, it is also studied quantity and distribution of pores, kerogen and fractures before compression and quantity and distribution of fractures after compression using Synchrotron X-ray Micro-Tomography (SYN-MCT) by segmentation program.

4.1 Radiograph images

The radiograph images from SYN-XRD in Table 4.1 on detector screen represent strain of sample varied anvils status. In some cases of releasing stress from the anvils, it brings about fractures development within the samples.

Strain of samples have been increased and decreased because there are pulling and pushing states of anvils.

Time Periods	Radiographic Images
002	

003	
004	
005	
006	





007	
008	
009	
010	

Table 4.1 shows radiographic images upon time periods.

We calculate %Strain using this equation;

$$\%Strain = \frac{Original\ length - Final\ length}{Original\ length} \times 100$$

those parameters in above equation are defined in Figure 4.1.

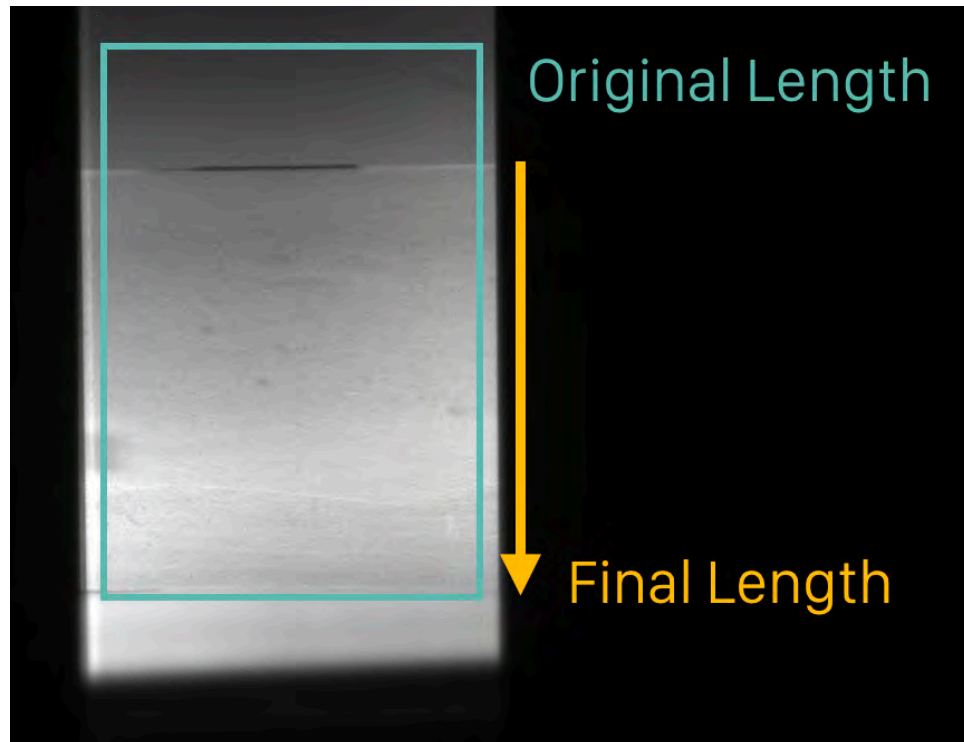


Figure 4.1 shows parameters used for calculating %Strain.

And here are results for %strain calculation (Table 4.2) and can plot %strain versus time periods showing compressional state (Figure 4.2).

Time periods	%Strain
002	0
003	5
004	17
005	30
006	27
007	15
008	30
009	15
010	12

Table 4.2 shows %Strain of each time period.

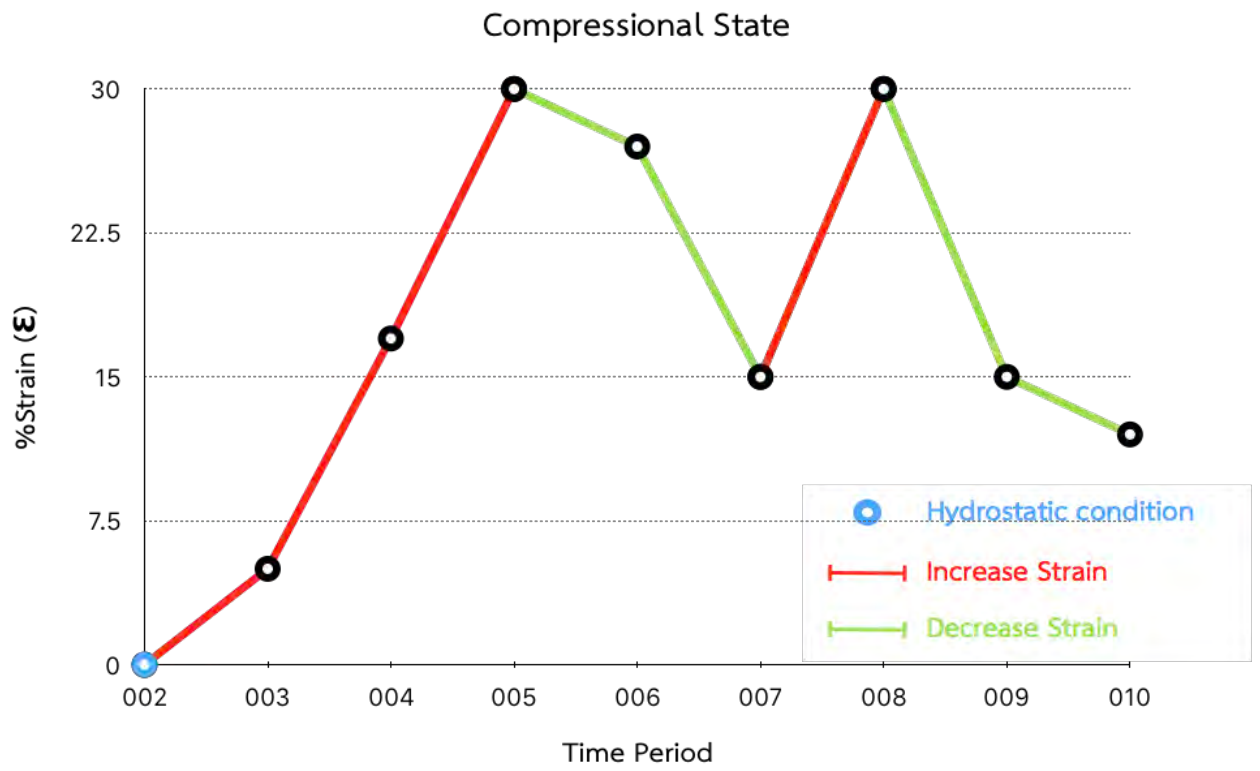


Figure 4.2 shows graph of compressional state and %Strain versus time periods.

4.2 Plot and Plot 2D

The results from MAUD software show 1D X-ray diffraction pattern and 2D Plot of time period 001 show in Figure 4.3.

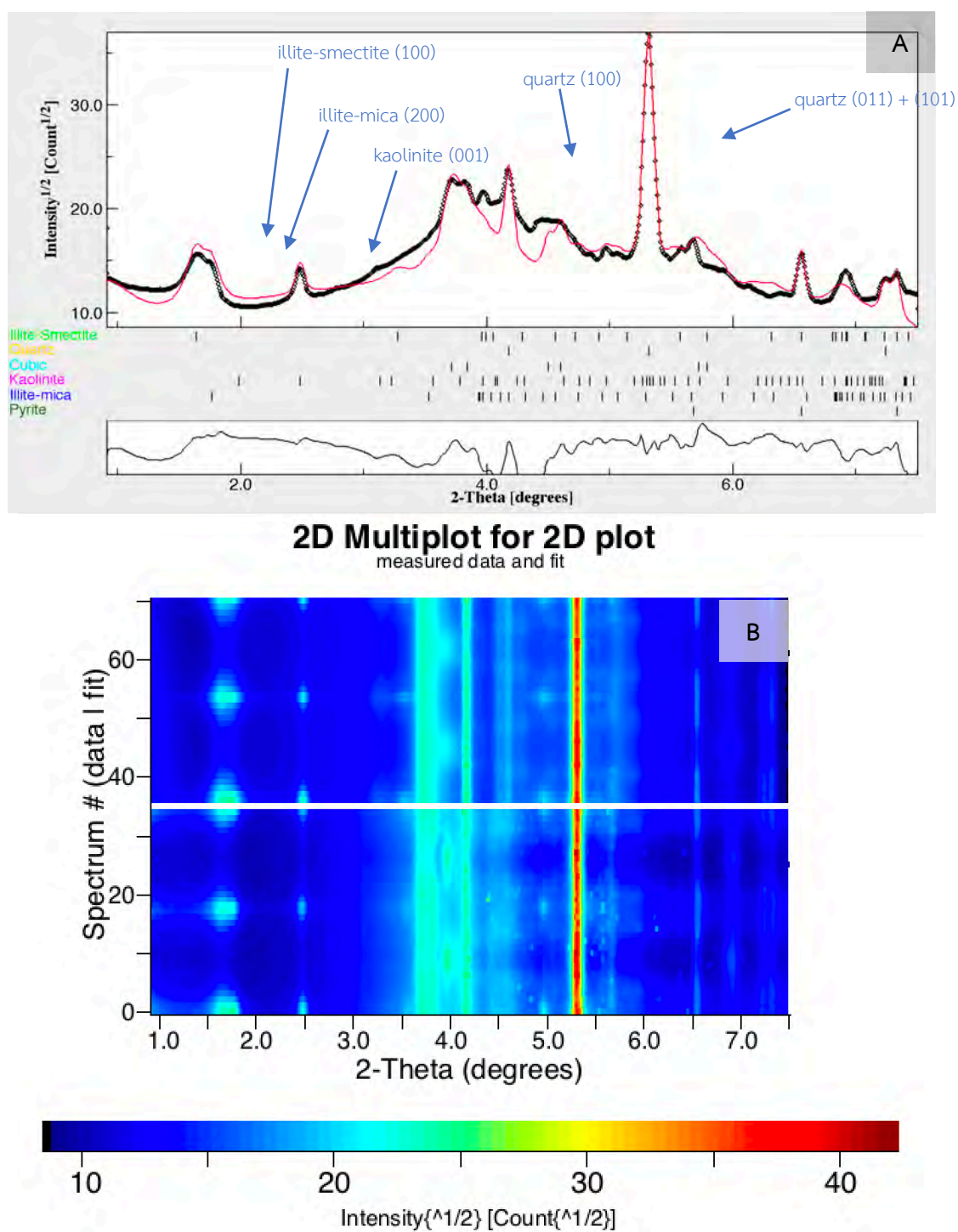


Figure 4.3 shows 1D X-ray diffraction pattern (A) and 2D Plot (B) of time period 001.

4.3 Mineralogy

The major phases in this study are; (1) illite-mica, (2) illite-smectite, and (3) Quartz. Kaolinite and Pyrite are minor phases. See more detail in Table 4.3.

Time periods	%Strain	illite-mica	illite-smectite	kaolinite	quartz	pyrite
001	0	27.73	25.46	2.80	34.57	9.44
002	0	37.44	22.05	3.41	32.29	4.80
003	5	35.61	21.00	4.82	31.58	6.97
004	17	43.27	20.63	3.92	25.44	6.74
005	30	38.65	21.97	3.62	29.95	5.81
006	27	43.27	19.92	3.85	21.52	11.44
007	15	45.74	18.64	4.16	23.15	8.31
008	30	43.70	17.25	4.27	29.20	5.57
009	15	36.93	14.86	3.43	36.10	8.68
010	12	47.21	11.81	3.58	31.78	5.61

Table 4.3 The detail of phase volume and weight fraction of those samples.

4.4 Cell parameters

Because compression condition made changing of cell parameter following Table 4.4.

Time periods	%Strain	illite-mica	illite-smectite	kaolinite	quartz		pyrite
		a (°A)	a (°A)	c (°A)	a (°A)	c (°A)	a (°A)
001	0	20.226	11.047	7.391	4.907	5.406	5.420
002	0	20.236	10.967	7.394	4.905	5.405	5.412
003	5	20.215	10.927	7.388	4.906	5.402	5.418
004	17	20.220	10.971	7.388	4.907	5.395	5.419
005	30	20.157	10.883	7.386	4.907	5.390	5.418
006	27	20.292	11.012	7.410	4.914	5.397	5.421
007	15	20.997	11.012	7.410	4.912	5.400	5.421
008	30	20.223	10.975	7.385	4.892	5.404	5.419
009	15	20.363	10.955	7.385	4.913	5.416	5.423
010	30	20.368	10.955	7.412	4.915	5.394	5.419

Table 4.4 shows parameters of cell parameter.

4.5 Preferred orientation

Generally, clay minerals are sheet silicate. They always have preferred orientation of their own seeing in pole figure with unit of multiples of a random distribution (m.r.d.). For illite-smectite and illite-mica, their strongly pole figure is (100). Kaolinite's pole figure is (001). Pyrite and quartz have a random orientation distribution. See more detail in Table 4.5.

Time periods	illite-mica		illite-smectite		kaolinite	
	Min	Max	Min	Max	Min	Max
001	0.135	6.177	0.531	3.440	0.337	8.554
002	0.546	4.968	0.415	2.942	0.125	8.319
003	0.494	4.907	0.455	2.526	0.496	7.080
004	0.579	4.432	0.286	2.609	0.422	7.522
005	0.526	4.668	0.502	2.433	0.441	7.687
006	0.503	4.466	0.467	2.234	0.345	6.602
007	0.519	3.565	0.407	2.174	0.309	5.063
008	0.526	4.197	0.429	2.048	0.494	6.814
009	0.522	3.519	0.545	2.365	0.372	5.472
010	0.560	3.394	0.580	2.150	0.496	5.152

Table 4.5 shows Pole densities for (100) pole figures of illite-mica and illite-smectite and (001) pole figure of kaolinite (m.r.d.)

4.6 Macrostress and differential stress

The Sinusoidal variations in peak position with azimuthal angles are result from differential stress which is defined as differential value of maximum stress and minimum stress, but they also are depended on mineral's elastic coefficients which are input in the refinement.

We investigate differential stress of each mineral from the sinusoidal variations using Moment pole stress method (Matthies *et al.*, 2001; Wenk *et al.*, 2014). we can calculate differential stress (t) from macrostress₁₁ following this equation.

$$t = (-3) \times \text{macrostress}_{11}$$

So, differential stress of each mineral on each time period can be calculated. But in this study we did not investigate differential stress of pyrite because there is few proportion. See more detail in Table 4.6.

Time periods	illite-mica		illite-smectite		kaolinite		quartz	
	D ₁₁ (GPa)	t (GPa)	D ₁₁ (GPa)	t (GPa)	D ₁₁ (GPa)	t (GPa)	D ₁₁ (GPa)	t (GPa)
002	-0.068	0.203	-0.470	1.411	0.006	-0.019	0.049	-0.146
003	-0.084	0.252	-0.628	1.884	0.007	-0.020	0.147	-0.441
004	-0.103	0.310	-0.878	2.634	0.010	-0.029	0.163	-0.503
005	-0.111	0.334	-0.771	2.313	0.033	-0.099	0.182	-0.546
006	-0.133	0.400	-0.818	2.454	-0.025	0.074	0.038	-0.115
007	-0.030	0.091	-0.926	2.778	-0.039	0.117	0.011	-0.033
008	-0.092	0.277	-0.819	2.456	-0.004	0.012	0.136	-0.408
009	-0.058	0.175	-0.947	2.842	-0.190	0.569	0.035	-0.105
010	-0.132	0.397	-1.010	3.031	0.002	-0.007	0.050	-0.150

Table 4.6 shows differential stress of minerals upon time periods.

4.7 Elastic property

So, we can plot stress-strain diagram of each mineral by plot a graph between differential stress (Y axis) and %Strain (X axis) (Figure 4.4).

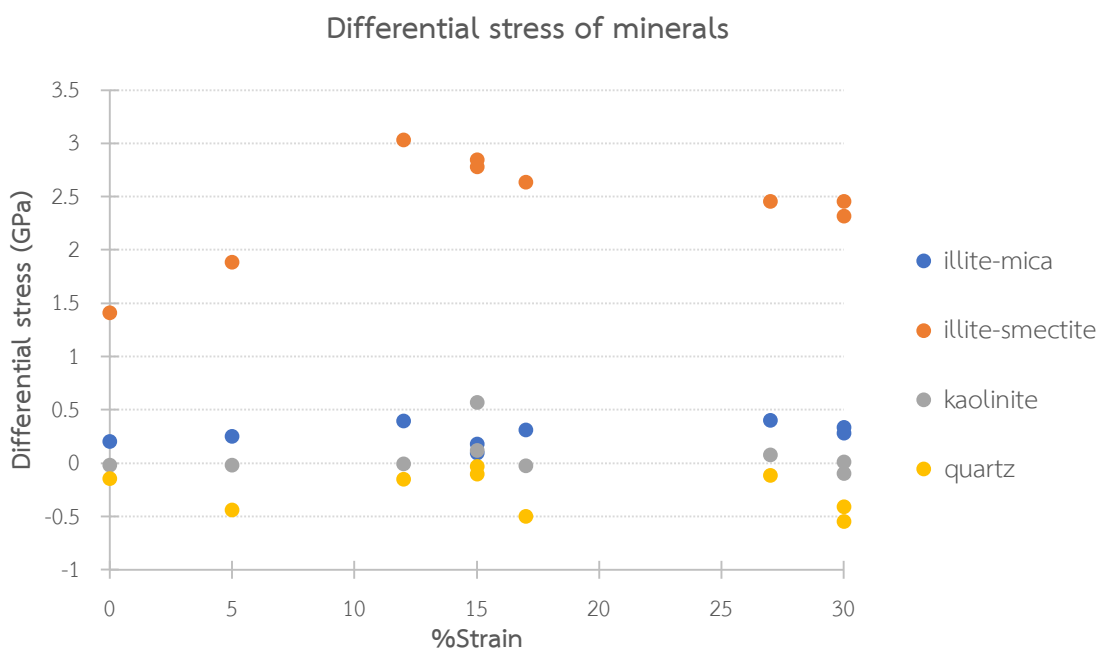


Figure 4.4 shows graph plotted values between differential stress (GPa) and %Strain.

4.8 Three-dimensional microstructure

From segmentation program, here are 2D segmented images showing their microstructures and textures before (Figure 4.5) and after (Figure 4.6) compression.

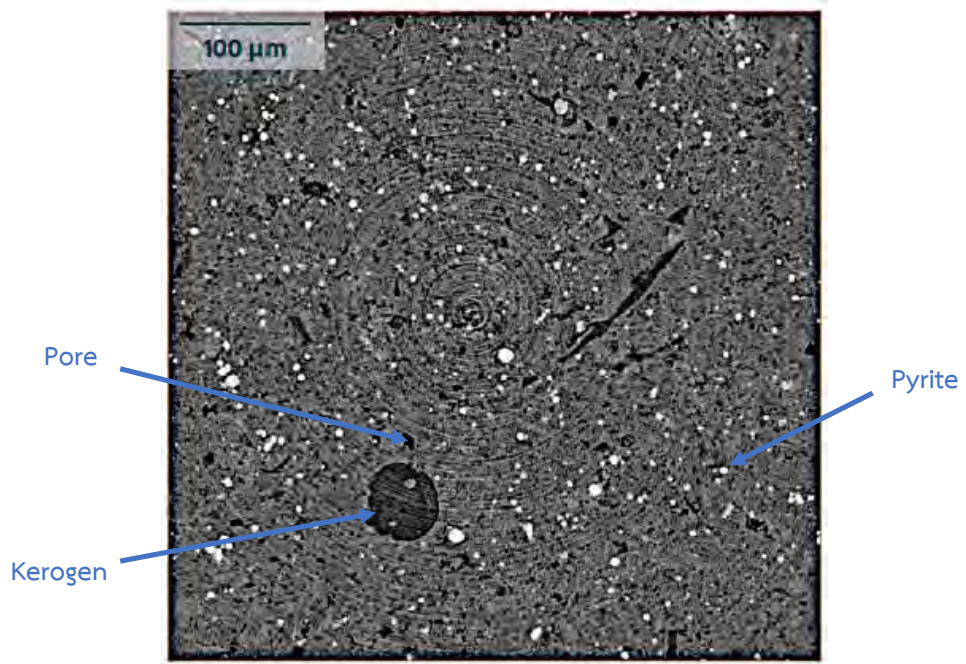


Figure 4.5 shows microstructures and textures before compression composing of pores, kerogen, and pyrite.

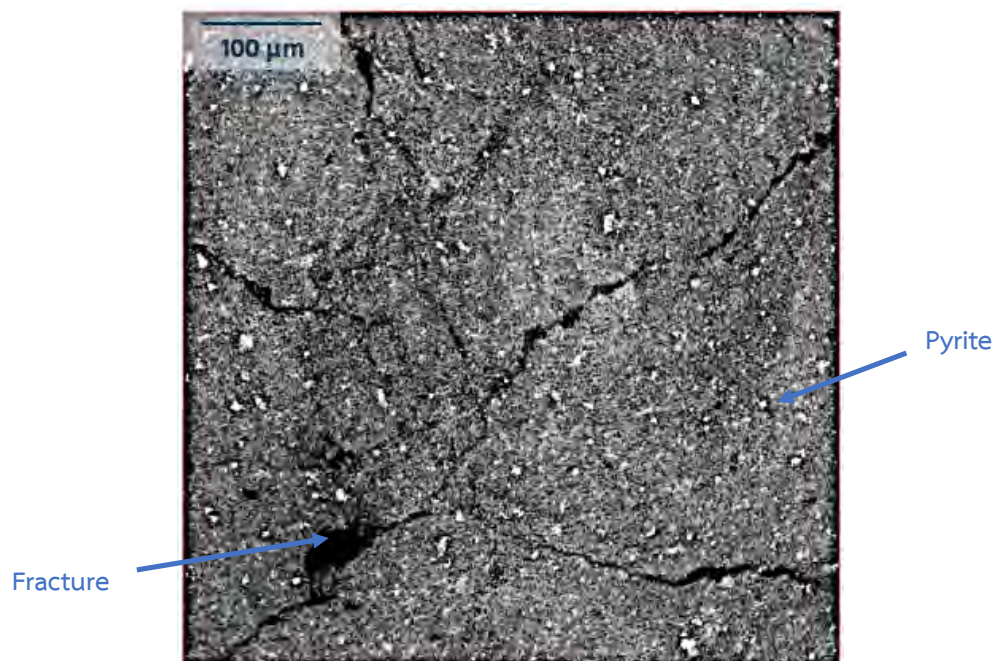


Figure 4.6 shows microstructures and textures after compression composing of fractures and pyrite.

And here are 3D mathematic simulation microstructure models before (Figure 4.7) and after (Figure 4.8) compression.

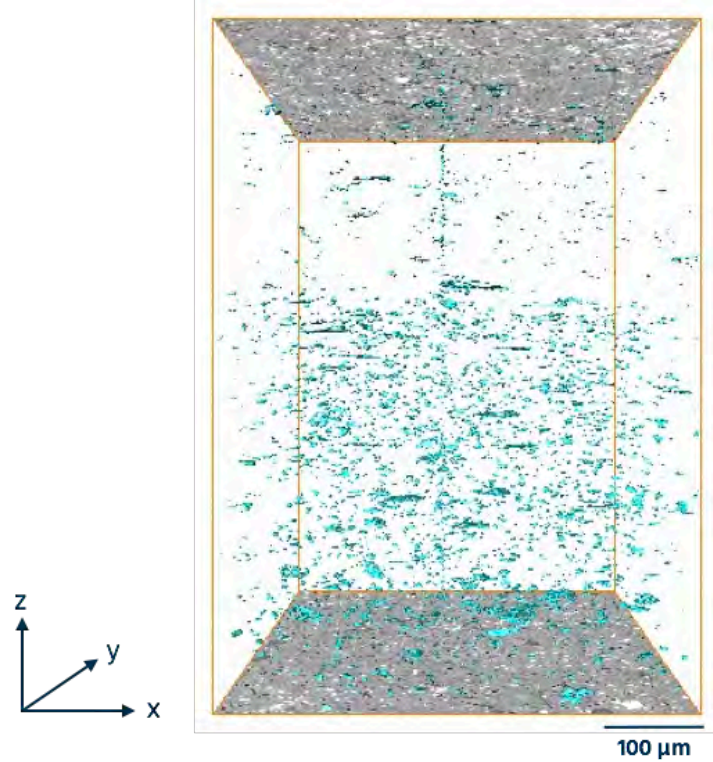


Figure 4.7 shows 3D microstructure model before compression which composes of scattered pores.

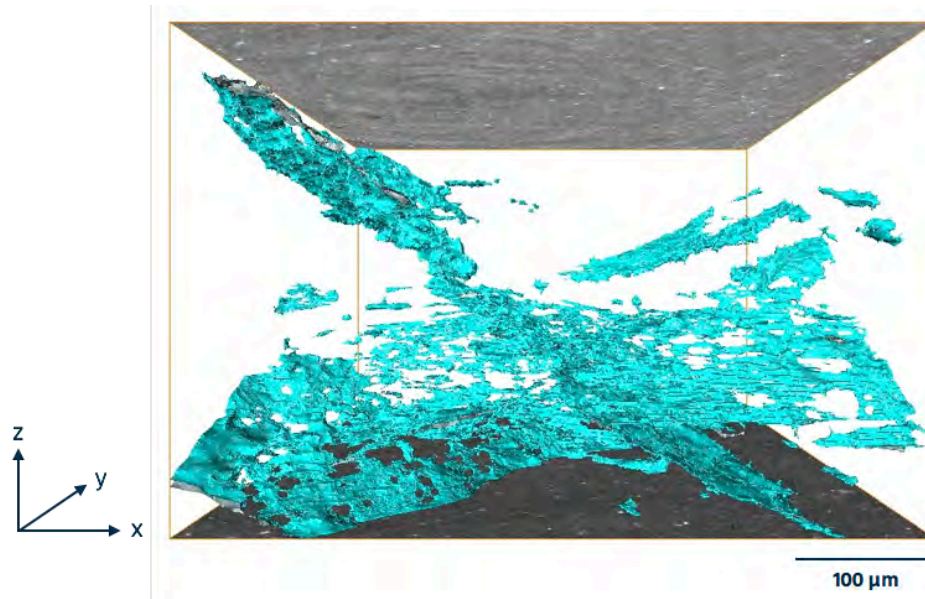


Figure 4.8 shows 3D microstructure model after compression which composes of huge fractures (Pores are not shown in this picture).

Moreover, from the segmentation program can also calculate proportion of pores, fractures, and kerogen. Before compression, there are pores 3.29% which are mostly rounded and scattered in the sample, fractures less than 0.1%, and kerogen 14.81% which is mostly aligned parallel with pores. After compression, there are decreasing of pores to 0.24%, increasing of fractures 1.27%. But we cannot determine exact volume of kerogen due to our sample is heated for a long time. So, kerogen is pyrolysis. See more detail in Figure 4.9.

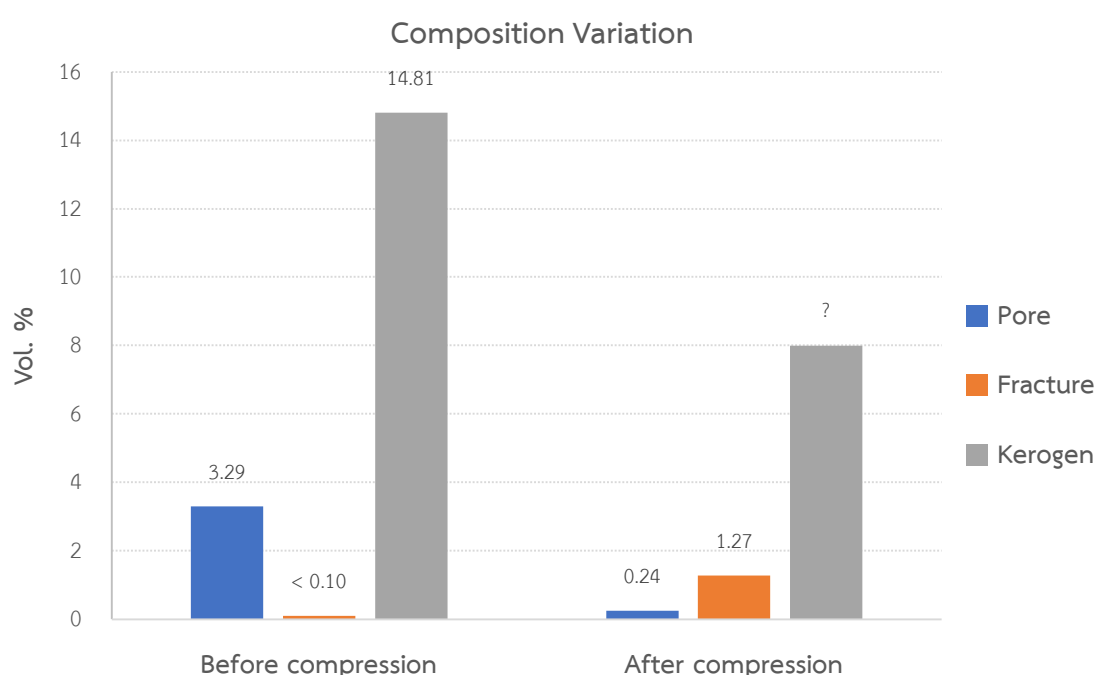


Figure 4.9 shows composition variation before and after compression.

4.9. Permeability from 3D mathematic simulation microstructure model

After we applied axis connectivity and absolute permeability experiment simulation functions in segmentation program to after compression's data, we got permeability values of x and y axis (Table 4.7).

	Permeability of x axis (md)	Permeability of y axis (md)
Before compression	0	0
After compression	9.31	6.38

Table 4.7 shows permeability of x and y axis.

CHAPTER V

DISCUSSION AND CONCLUSIONS

5.1. Discussion

5.1.1. Proportion of illite-mica and illite-smectite

The transition series of illite-smectite to illite-mica occurs due to increasing temperature. The transition process is known as illitization which has been documented in low-temperature environments and is generally associated with burial diagenesis, low-grade metamorphism, contact metamorphism, and hydrothermal alteration (Bauluz, 2007).

Hower *et al.*, 1976 suggest that the illitization process produces loss of Si, Na, and H₂O and gain of K and Al.

In this study, our sample had been heated for a long time, illite-smectite which have water (H₂O) in the chemical formula is dehydrated and changed its phase to become illite-mica. The proportion of illite-mica increases while the proportion of illite-smectite decreases over time (Figure 5.1).

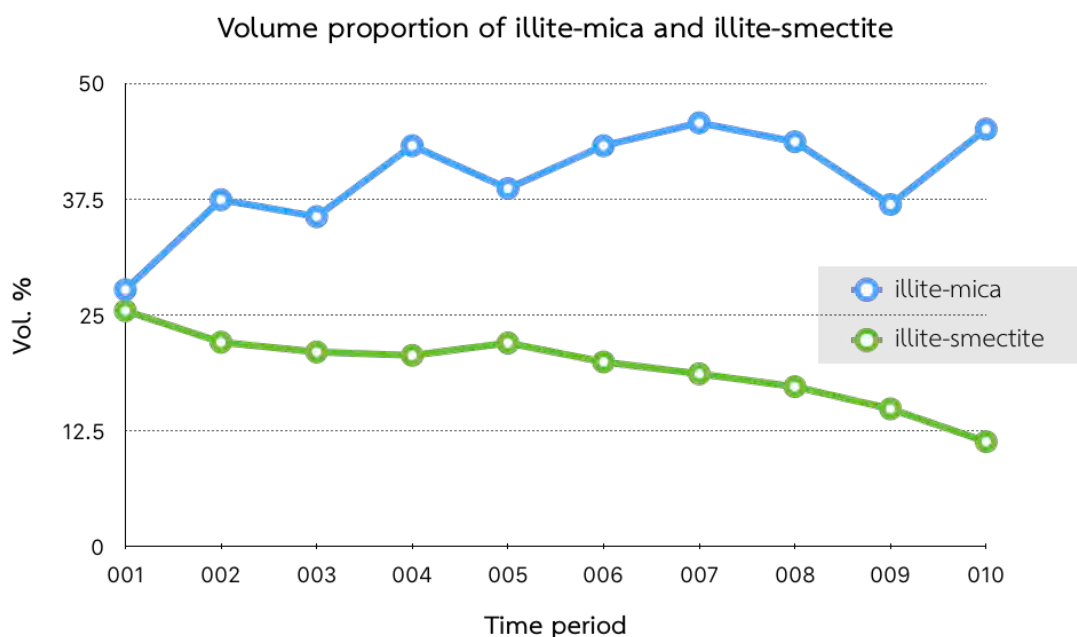


Figure 5.1 shows graph of vol.% of illite-mica and illite-smectite.

5.1.2. Stiffness of minerals

Object is deformed when stresses act on it. But how much of its deformations is depended on its stiffness.

First of all, stiffness can be defined as the resistance of an elastic body to deformation by an applied force. It means that if there are 2 minerals; A and B. If we apply a force to mineral A, and it easily deforms (high strain). The mineral A is less stiffness. On the other hand, if we apply the same force to mineral B, and it hardly deforms (less strain). The mineral B is high stiffness.

We use this concept to determine the stiffness of our composed minerals following Figure 4.4.

We can conclude that illite-smectite is the least stiff. Whereas quartz is the most stiff one.

5.1.3. Fracture development

The fracture development in this study can be explained by radiographic images from SYN-XRD. We define fracture development into 4 state;

(1) Closure of existing cracks aligning parallel with bedding plane and scattered pores in the initial state of compression (Figure 5.2). In this state makes the proportion of pores decrease from 3.29 Vol.% before compression to 0.24 Vol.% after compression (Figure 4.9).

(2) Growth of cracks oblique to the bedding plane in the middle to late of compression (Figure 5.3)

(3) cracks connection from grown cracks in the second state in the late of compression (Figure 5.4)

(4) fractures observed, permeability increases (Figure 5.5) due to unloading of anvils, pressure is decreased. Remind that bedding plane is aligned horizontally (light blue).

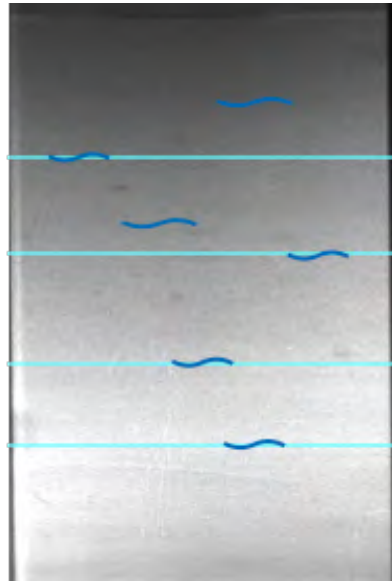


Figure 5.2 shows the first state of fracture development: Closure of existing cracks (dark blue).



Figure 5.3 shows the second state of fracture development: growth of cracks (red).



Figure 5.4 shows the third state of fracture development: cracks connection (red).



Figure 5.5 shows the third state of fracture development: fractures observed (red), permeability increases.

Moreover, the proportion of kerogen after compression decreases due to our sample had been heated for a long time thus kerogen is pyrolysis. But we cannot determine exact volume because thermal energy makes atoms vibrate. So, the contrast of absorption values between kerogen and fracture are not much different due to their vibration.

5.1.4. Fracture angle

Once fractures are observed, we can measure angle between fractures and bedding plane which aligns horizontally in the same direction on the stress.

The Mohr-Coulomb criterion predicts a shear plane angle oblique to the direction of the major principle stress of homogeneous rock which have average about 33° .

Zhang (2015) also studied the stress-strain-permeability behaviour of clay rock during damage and recompaction experimentally in triaxial compression. He also measured angle of his compressed rock averaging about $27^\circ \pm 4^\circ$ (Figure 5.6).

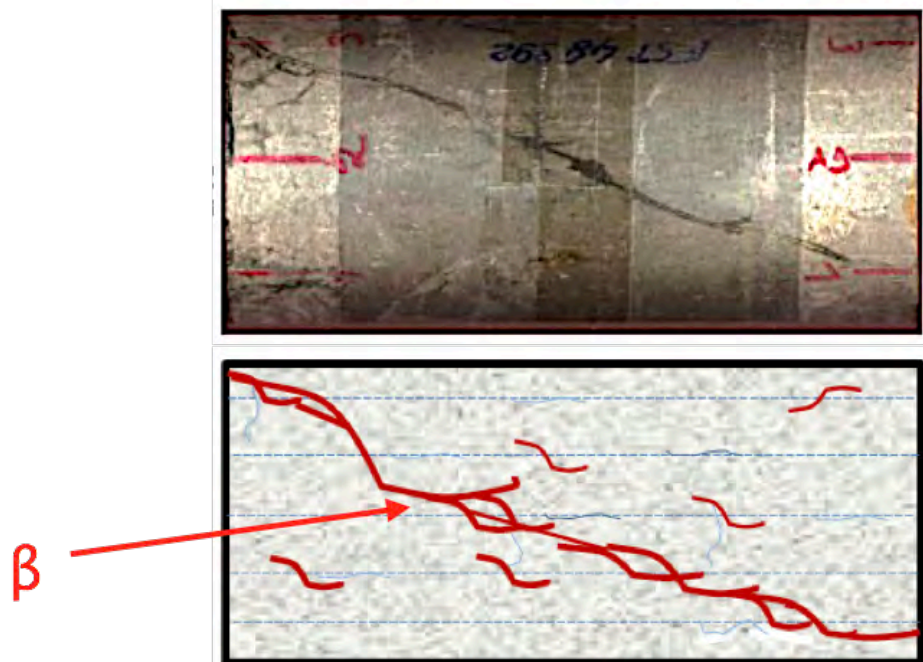


Figure 5.6 shows angle between fractures and major principle stress (Zhang, 2015).

In this study, we also measured angle between fractures and major principle stress which is as same as to the direction of bedding plane. The average of angle is about $26^\circ \pm 3^\circ$ (Figure 5.7).

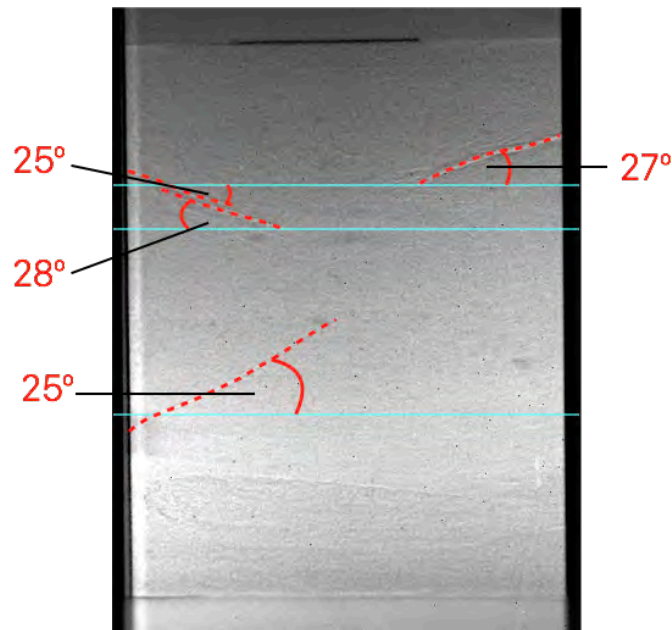


Figure 5.7 shows angle between fractures and major principle stress of this study.

Our averaged angle is smaller than the Mohr-Coulomb criterion and Zhang (2015) due to our sample composes of clay minerals over 50% which are sheet silicate mineral aligning horizontally with bedding plane. Thus, the fractures are easier to develop parallel with bedding plane which is the weakest direction of the sample but they are also controlled by the anvils of D-DIA.

5.2. Conclusions

Our shale sample from the Barnett Shale, Texas, USA composes of quartz (~35%), illite-mica (~28%) illite-smectite (~25%), pyrite (~9%), and kaolinite (~3%). Upon compressing sample, the volumes of illite-smectite decrease due to dehydration whereas the volumes of illite-mica increase. Moreover, diffraction patterns from SYN-XRD also suggest that illite-smectite is the least stiff mineral. On the other hand, quartz is the most stiff one.

Before compression, there are scattered pores (~3%) all of the sample, fractures (< 0.1%), and kerogen (~15%) aligning parallel with pores. Upon compressing sample, pores decrease. After compression, there are pores (~0.2%), fractures (~1.3%), and kerogen which is cannot determined exact volumes.

In this study can define development of fracture into 4 states which are;

- (1) Closure of existing cracks and scattered pore.
- (2) Growth of cracks
- (3) Cracks connection
- (4) Fractures observed, permeability increases

Newly develop fractures mostly intersect with the bedding plane at the average of 26° due to the change of stress-strain state from unloading and they increase permeability of the sample ranging from 6.4 to 9.3 mD.

The results from this study make knowledge in fractures behavior and their development in extreme condition be better understood and can also apply for study about fractures development of shale in the other basins in the future.

REFERENCES

- Bauluz B.L., (2007). Illitization processes: Series of dioctahedral clays and mechanisms of formation, *Sociedad Espanola de Mineralogia*, 3, 31-39.
- Bowker, K. A. (2003). Recent development of the Barnett Shale play, Fort Worth Basin, *West Texas Geological Society Bulletin*, 42(6), 4-11.
- Burgess, W.J. (1976). Geologic evolution of mid-continent and Gulf Coast areas; plate tectonics view. *Gulf Coast Association of Geological Societies Transactions*, 26, 132–143.
- Cnudde, V., & Boone, M.N. (2013). High-resolution X-ray computed tomography in geosciences: a review of the current technology and applications. *Earth Science Reviews*.
- Henry, J.D. (1982). Stratigraphy of the Barnett Shale (Mississippian) and associated reefs in the northern Fort Worth Basin; in Martin C.A., ed., *Petroleum geology of the Fort Worth Basin and Bend arch area. Dallas Geological Society*, 157–178.
- Herkommer, M.A. & Denke, G.W. (1982). Stratigraphy and hydrocarbons, Parker County, Texas, in Martin C.A., ed., *Petroleum geology of the Fort Worth Basin and Bend arch area. Dallas Geological Society*, 97–127.
- Heyliger, P., Ledbetter H., & Kim., S. (2003). Elastic constants of natural quartz. *Journal of the Acoustical Society of America*, 114(2), 644-650.
- Hower, J., Eslinger, E.V., Hower, M.E., & Perry, E.A. (1976). Mechanism of burial metamorphism of argillaceous sediment: 1. Mineralogical and chemical evidence. *Geological Society of America Bulletin*, 87, 725–737.
- IHS Energy, 2003, U.S. production and well history control databases, Englewood, Colorado.
- Jarvie, D.M., Hill, R.J., Pollastro, R.M., Wavrek, D.A., Bowker, K.A., Claxton, B.L., & Tobey, M.H. (2003). Evaluation of unconventional natural gas prospects: The Barnett Shale fractured shale gas model (abs.): 21st International Meeting on Organic Geochemistry, September 8 –12, 2003, Krakow, Poland, 2, 3–4.
- Jarvie, D.M., Hill, R.J., Pollastro, R.M., Wavrek, D.A., Bowker, K.A., Claxton, B.L., & Tobey, M.H. (2004a). Assessment of the gas potential and yields from shales: The Barnett Shale model: Unconventional Gas of the Southern Mid-Continent Symposium Program and Abstracts, March 9–10, 2004, Oklahoma City, Oklahoma.
- Jarvie, D.M., Hill, R.J., & Pollastro, R.M. (2005). Assessment of the gas potential and yields from shales: The Barnett Shale model, in Cardott B.J., ed., *Unconventional energy*

- resources in the southern midcontinent, 2004 symposium. *Oklahoma Geological Survey Circular*, 110, 37–50.
- Kaercher, P.M., Zepeda-Alarcon, E., Prakapenka, V.B., Kanitpanyacharoen, W., Smith, J.S., Sinogeikin, S., & Wenk, H.-R. (2014). Preferred orientation in experimentally deformed stishovite: implications for deformation mechanisms. *Physics and Chemistry of Minerals*, 42, 275–285.
- Kanitpanyacharoen, W., Wenk, H.-R., Kets, F., Lehr, C., & Wirth, R. (2010). Texture and anisotropy analysis of Qusaiba shales. *Geophysical Prospecting*, 59, 536-556.
- Kanitpanyacharoen, W., Merkel, S., Miyagi, L., Kaercher, P.M., Tomé C.N., Wang, Y., & Wenk, H.-R. (2011). Significance of mechanical twinning in hexagonal metals at high pressure. *Acta Materialia*, 60, 430-442.
- Kanitpanyacharoen, W., Kets, F.B., Wenk, H.-R., & Wirth, R. (2012). Mineral preferred orientation and microstructure of Posidonia Shale in relation to different degrees of thermal maturity. *Clays and Clay Minerals*, 60(3), 315-329.
- Kanitpanyacharoen, W., Parkinson, D.Y., Carlo, F.D., Marone, F., Stampanoni, M., Mokso, R., MacDowell, A., & Wenk, H.-R. (2013). A comparative study of X-ray tomographic microscopy on shales at different synchrotron facilities: ALS, APS and SLS. *Journal of Synchrotron Radiation*, 20, 172-180.
- Kanitpanyacharoen, W., Vanorio, T., Xiao, X., & Liu, Y. (2015). Evolution of microstructures in Kimmeridge shale upon thermally-induced kerogen maturation. *Journal of Geophysical Research*.
- Kawazoe, T., Nishiyama, N., Nishihara, Y., & Irifune, T. (2010). Pressure generation to 25 Gpa using a cubic anvil apparatus with a multi-anvil 6-6 assembly, *High Pressure Research*, 30(1), 161-174.
- Kerans, C. (1988). Karst-controlled reservoir heterogeneity in Ellenburger Group carbonates of west Texas. *AAPG Bulletin*, 72, 1160–1183.
- Kinney, J.H., & Nichols, M.C. (1992). X-ray tomographic microscopy (XTM) using synchrotron radiation. *Annual Review of Materials Science*, 22, 121-152.
- Lutterotti, L. & Scardi, P. (1990). Simultaneous structure and size-strain refinement by the Rietveld method. *Journal of Applied Crystallography*, 23, 246-252.
- Lutterotti, L., Matthies S., Wenk, H.-R., Schultz, A.S., & Richardson Jr., J.W. (1997). Combined texture and structure analysis of deformed limestone from time-of-flight neutron diffraction spectra. *Journal of Applied Physics*, 81(2), 594-600.

- Lutterotti, L., Vasin R., & Wenk, H.-R. (2013). Rietveld texture analysis from synchrotron diffraction images. I. Calibration and basic analysis, *Powder Diffraction*, 29(1), 76-84.
- Mapel, W.J., Johnson, R.B., Bachman, G.O., & Varnes, K.L. (1979). Southern midcontinent and southern Rocky Mountains region, in Craig L.C. and Connor C.W., coordinators, Paleotectonic investigations of the Mississippian system in the United States. *U.S. Geological Survey Professional Paper*, P1010, 161-187.
- Matthies, S. (1996). Moment pole figures in residual stress analysis. *Textures and Microstructures*, 25(2-4), 229-236.
- Matthies, S., Priesmeyer, H.G., & Daymond, M.R. (2001). On the diffractive determination of single-crystal elastic constants using polycrystalline samples. *Journal of Applied Crystallography*, 34, 585-601.
- Montgomery, S.L., Jarvie, D.M., Bowker, K.A., & Pollastro, R.M. (2006). Mississippian Barnett Shale, Fort Worth Basin: Northcentral Texas: Gas-shale play with multi-tcf potential, reply. *AAPG Bulletin*, 90, p. 967-969.
- Pollastro, R.M. (2003) Geologic and production characteristics utilized in assessing the Barnett Shale continuous (unconventional) gas accumulation, Barnett-Paleozoic total petroleum system, Fort Worth Basin, Texas: Barnett Shale Symposium, Ellison Miles Geotechnology Institute at Brookhaven College, Dallas, Texas, November 12-13, 2003, 6 p.
- Pollastro, R.M., Hill, R.J., Jarvie, D.M., & Adams, C. (2004a). Geologic and organic geochemical framework of the Barnett- Paleozoic total petroleum system, Bend arch-FortWorth Basin, Texas (abs.). *AAPG Annual Meeting Program*, 13, A113.
- Pollastro, R.M., Jarvie, D.M., Hill, R.J., & Adams, C.W. (2007). Geological framework of the Mississippian Barnett Shale, Barnett-Paleozoic total petroleum system, Bend arch - Fort Worth Basin, Texas. *AAPG Bulletin*, 91(4), 405-436.
- Rietveld, H.M. (1964) A profile refinement method for nuclear and magnetic structure. *Journal of Applied Crystallography*, 2, 65-71.
- Singh, A.K. (1993). The lattice strains in a specimen (cubic system) compressed nonhydrostatically in an opposed anvil device. *Journal of Applied Physics*, 73, 4278-4286.
- Singh, A.K., Balasingh, C., Mao, H.K., Hemley, R.J., & Shu, J. (1998). Analysis of lattice strains measured under nonhydrostatic pressure. *Journal of Applied Physics*, 83(12), 7567-7575.
- Singh, A.K., Mao, H.-K., Shu, J., & Hemley, R.J. (1998). Estimation of single-crystal elastic moduli from polycrystalline X-ray diffraction at high pressure: application to FeO and iron. *Physical Review Letter*, 80, 2157-2160.

- Sloss, L.L. (1976). Areas and volumes of cratonic sediments, western North America and Eastern Europe. *Geology*, 4, 272–276.
- Sone, H., & Zoback M.D. (2013). Mechanical properties of shale-gas reservoir rocks - Part 1: Static and dynamic elastic properties and anisotropy. *Geophysics*, 78(5), 381-392.
- Texas Railroad Commission. (2003). Devon Energy Operating Co. Hearing: Docket No. 05, 7B, and 09-0235294, July 15, 2003, 55 exhibits.
- Thompson, D.M. (1982) Atoka Group (lower to middle Pennsylvanian), northern Fort Worth Basin, Texas: Terrigenous depositional systems, diagenesis, and reservoir quality: University of Texas, Bureau of Economic Geology, Report of Investigations, 125, 62 p.
- Thompson, D.M. (1988). Fort Worth Basin; in Sloss L.L., ed., *The geology of North America: Geological Society of America*, D-2, 346–352.
- Turner, G.I. (1957). Paleozoic stratigraphy of the Fort Worth Basin, in W. C. Bell, ed., *Abilene and Fort Worth Geological Societies Joint Field Trip Guidebook*, 57–77.
- Vasin, R.N., Wenk, H.-R., Kanitpanyacharoen W., Matthies S., & Wirth, R. (2013). Elastic anisotropy modeling of Kimmeridge shale, *Journal of Geophysical Research: Solid Earth*, 118, 3931-3956.
- Walls, J.D., Diaz, E., & Cavanaugh, T. (2012). Shale Reservoir Properties from Digital Rock Physics. SPE 152752. In: 2012 The SPE/EAGE European Unconventional Resources Conference and Exhibition held in Vienna, Austria.
- Walper, J.L. (1977). Paleozoic tectonics of the southern margin of North America, *Gulf Coast Association of Geological Societies Transactions*, 27, 230–239.
- Walper, J.L. (1982). Plate tectonic evolution of the Fort Worth Basin, in Martin C.A., ed., *Petroleum geology of the Fort Worth Basin and Bend arch area: Dallas Geological Society*, 237-251.
- Wang, Y., Durham, W.B., Getting, I.C., & Weidner, D.J. (2013). The deformation-DIA: A new apparatus for high temperature triaxial deformation to pressures up to 15 GPa. *Review of Scientific Instruments*, 74(6), 3002-3011.
- Wenk, H.-R., Voltolini, M., Kern, H., Popp, T., & Mazurek, M. (2008). Anisotropy in shale from Mont Terri. *The Leading Edge*, 27(6), 742-748.
- Wenk, H.-R., Lutterotti L., Kaercher, P., Kanitpanyacharoen, W., Miyagi, L., & Vasin, R. (2014). Rietveld texture analysis from synchrotron diffraction images: II, Complex multiphase materials and diamond anvil cell experiments. *Powder Diffraction*, 29(3), 220-232.
- Zhang, C.-L. (2015). The stress-strain-permeability behaviour of clay rock during damage and recompaction. *Journal of Rock Mechanics and Geotechnical Engineering*, 8, 16-26.